ADVANCED MATERIALS
www.advmat.de

"Cut-and-Paste" Manufacture of Multiparametric Epidermal Sensor Systems

*Shixuan Yang, Ying-Chen Chen, Luke Nicolini, Praveenkumar Pasupathy, Jacob Sacks, Su Becky, Russell Yang, Sanchez Daniel, Yao-Feng Chang, Pulin Wang, David Schnyer, Dean Neikirk, and Nanshu Lu**

Our body is radiating data about ourselves continuously and individually. Wearable devices that can pick up and transmit signals from the human body have the potential to transform mobile health (mHealth) and human–machine interface (HMI), which prompted the Forbes Magazine to name 2014 as the year of wearable technology.[1] However, since wafer-based integrated circuits are planar, rigid, and brittle, state-of-the-art wearable devices are mostly in the form factors of "chips on tapes" or "bricks on straps," which are unable to maintain intimate and prolonged contact with the curved, soft, and dynamic human body for long-term, high-fidelity physiological signal monitoring.[2]

Recent advancements in flexible and stretchable electronics have provided viable solutions to bio-mimetic electronic skins[3–5] and bio-integrated electronics.[6,7] Among many breakthroughs, epidermal electronic systems (EES) represent a paradigm-shift wearable device whose thickness and mechanical properties can match that of human epidermis.[8] As a result, the EES can conform to human skin like a temporary transfer tattoo and deform with the skin without detachment or fracture. The EES was first developed to monitor electrophysiological (EP) signals,[8] and thereafter skin temperature,[9,10] skin hydration,[11–13] sweat,[14,15] and even movement disorders.[16] Moreover, near field communication (NFC) antenna based on EES technology has also been reported.[13,15,17]

The thinness and softness of EES, however, lead to collapsing and crumpling after it is peeled off human skin, making its use as a disposable electronic tattoo ideal. As a result, the success of EES hinges on the realization of low-cost, high-throughput manufacture. Current EES manufacture relies on standard microelectronics fabrication processes including vacuum deposition of films, spin coating, photolithography, wet and dry etching, as well as transfer-printing.[8,13,17] Although it has been proved effective, there are several limitations associated with such process: first, a rigid handle wafer has to be used for photolithography, making it incompatible with roll-to-roll process; second, the high cost associated with cleanroom facilities, photo masks, photolithography chemicals, and manpower prevents EES from being inexpensive and disposable; third, high vacuum film deposition is time consuming and hence impractical for growing thick films; fourth, the EES size is confined by the size of the handle wafer, whose size is limited by the smallest vacuum chamber throughout the process; and last but not least, the high manpower demand of the manufacturing process greatly limits the accessibility of EES.

Our newly invented "cut-and-paste" method offers a very simple and immediate solution to the above mentioned challenges. Instead of high vacuum metal deposition, thin metal-on-polymer laminates of various thicknesses can be directly purchased from industrial manufacturers. Instead of using photolithography patterning, a benchtop programmable cutting machine is used to mechanically carve out the patterns as designed, with excess being removed, which is a freeform, subtractive manufacturing process, inverse to the popular freeform, additive manufacturing technology.[18] The cutting machine can pattern on thin sheet metals and polymers up to 12 inches wide and several feet long, largely exceeding lab-scale wafer sizes. Since the patterns can be carved with the support of thermal release tapes (TRTs), whose adhesive can be released after heating, the patterned films can be directly printed onto a variety of tattoo adhesives and medical tapes with almost 100% yield. The whole process can be completed on an ordinary bench within 10 min without any wet process, which allows rapid prototyping. Equipment used in this process only includes a desktop cutting machine for thin film patterning and a hot plate for TRT heating, which enables portable manufacture. Since no rigid handle wafer is needed throughout the process, the "cut-and-paste" method is intrinsically compatible with roll-to-roll manufacture. To demonstrate the "cut-and-paste" method, multimaterial epidermal sensor systems

S. Yang, Y.-C. Chen, L. Nicolini, J. Sacks, S. Becky, R. Yang, S. Daniel, Dr. Y.-F. Chang, Dr. P. Wang, Prof. N. Lu
Center for Mechanics of Solids, Structures and Materials
Department of Aerospace Engineering and Engineering Mechanics
University of Texas at Austin
Austin, TX 78712, USA
E-mail: nanshulu@mail.utexas.edu
Y.-C. Chen, P. Pasupathy, Dr. Y.-F. Chang, Prof. D. Neikirk
Department of Electrical and Computer Engineering
University of Texas at Austin
Austin, TX 78712, USA
L. Nicolini, Prof. N. Lu
Texas Materials Institute
University of Texas at Austin
Austin, TX 78712, USA
Prof. D. Schnyer
Department of Psychology
University of Texas at Austin
Austin, TX 78712, USA
Prof. N. Lu
Department of Biomedical Engineering
University of Texas at Austin
Austin, TX 78712, USA

DOI: 10.1002/adma.201502386

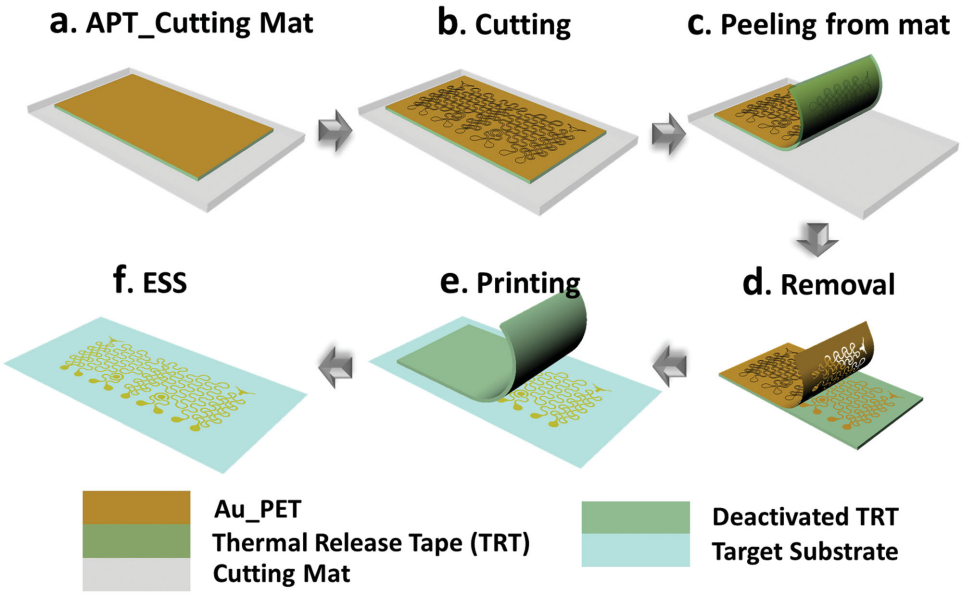

Figure 1. Schematics for the "cut-and-paste" process. a) Au-PET-TRT (APT) laminated on the cutting mat with PET being the topmost layer. b) Carving designed seams in the Au-PET layer by an automated mechanical cutting machine. c) Peeling APT off the cutting mat. d) Removing excessive Au-PET layer after deactivating the TRT on hot plate. e) Printing patterned Au-PET layer onto target substrate. f) Resulted epidermal sensor system (ESS) with Au being the topmost layer.

(ESS) are fabricated and applied to measure EP signals such as electrocardiogram (ECG), electromyogram (EMG), electroencephalogram (EEG), skin temperature, skin hydration, and respiratory rate. A planar stretchable coil of 9-μm-thick aluminum ribbons exploiting the double-stranded serpentine design is also integrated on the ESS as a MHz frequency, wireless strain gauge, which can also serve as NFC antenna in the future.

A schematic of the freeform "cut-and-paste" process is shown in **Figure 1**. Since stiff-polymer-supported blanket metal films are more stretchable than freestanding metal sheets,[19] we always use metal-on-stiff-polymer laminates as the starting materials. Starting materials such as gold (Au) coated polyimide and aluminum (Al) coated polyethylene terephthalate (PET) are commonly used as thermal control or cable shielding laminates and can be purchased from industrial suppliers such as Sheldahl (Northfield, MN) and Neptco (Pawtucket, RI). We were able to purchase a small roll of 9-μm-thick Al on 12-μm-thick PET laminates from Neptco. Since only a small amount of polymer-supported Au foils are used in this research but industrial quantity can be very expensive, we chose to use thermal evaporation to deposit several batches of 100-nm-thick Au films on 13-μm-thick transparent PET foils (Goodfellow, USA). A picture of the Au-on-PET foil is shown in Supporting Information Figure S1a. To manufacture Au-based stretchable EP electrodes, resistance temperature detectors (RTDs), and impedance sensors, the Au-on-PET foil was uniformly bonded to a flexible, single-sided TRT (Semiconductor Equipment Corp., USA) with Au side touching the adhesive of the TRT, as shown in Supporting Information Figure S1b. The other side of the TRT was then adhered to a tacky flexible cutting mat, as shown in Figure 1a and Supporting Information Figure S1c. The cutting mat was fed into a programmable cutting machine (Silhouette Cameo, USA) with the PET side facing the cutting blade. By importing our AutoCAD design into the Silhouette Studio software, the cutting machine can automatically carve the Au-on-PET sheet with designed seams within minutes (Figure 1b and Supporting Information Figure S1d). Once seams were formed, the TRT was gently peeled off from the cutting mat (Figure 1c and Supporting Information Figure S1e). Slightly baking the TRT on a 115 °C hotplate for 1–2 min (Supporting Information Figure S1f) deactivated the adhesives on the TRT so that the excesses can be easily peeled off by tweezers (Figure 1d and Supporting Information Figure S1g), leaving only the EP electrodes, RTD, and impedance sensors loosely resting on the TRT. The patterned devices were finally printed onto a target substrate with native adhesives, which could be a temporary tattoo paper (Silhouette) or a medical tape, such as 3M Tegaderm transparent dressing or 3M kind removal silicone tape (KRST) (Figure 1e and Supporting Information Figure S1h), yielding a Au-based ESS (Figure 1f and Supporting Information Figure S1i). Steps illustrated by Figure 1a–e can be repeated for other thin sheets of metals and polymers, which can be printed on the same target substrate with alignment markers, rendering a multimaterial, multiparametric ESS ready for skin mounting.

A multimaterial, multiparametric ESS supported by transparent temporary tattoo paper and its white liner is shown in **Figure 2**a, which includes three Au-based filamentary serpentine (FS) EP electrodes, one Au-based FS RTD, two Au-based dot-ring impedance sensors, and an Al-based planar stretchable coil. In this picture, all Au-based sensors have the Au side facing up and in the future touching human skin as Au is a biocompatible metal. The stretchable coil, however, has the blue colored PET facing up because PET has demonstrated good biocompatibility[20] but some people's skin can be allergic to Al. For the three EP electrodes, the interelectrode distance is

Adv. Mater. **2015**,
DOI: 10.1002/adma.201502386

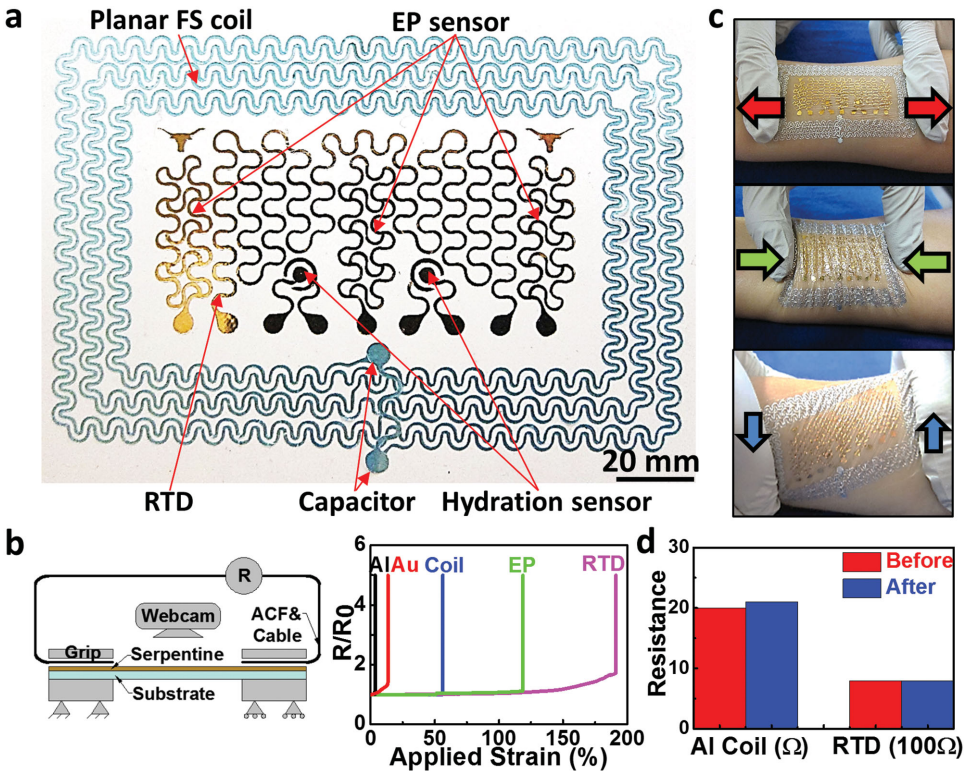

Figure 2. Multimaterial, multiparametric ESS. a) Top view of an ESS which incorporates three electrophysiological (EP) electrodes (Au-PET), a resistance temperature detector (RTD) (Au-PET), two coaxial dot-ring impedance sensors (Au-PET), and a wireless planar stretchable strain sensing coil (Al-PET), all in filamentary serpentine (FS) layout. b) Resistance change measured as function of applied strain. "Al" denotes straight Al-PET ribbon, "Au" denotes straight Au-PET ribbon, "Coil" denotes Al-PET serpentine ribbon used in wireless strain sensor coil, "EP" denotes Au-PET serpentine ribbon used in EP electrode, and "RTD" denotes Au-PET serpentine ribbon used in RTD. c) ESS on human skin demonstrating excellent deformability during stretch (top), compression (middle), and shear (bottom). d) Resistance of Al coil and Au RTD before and after all possible deformations of skin-mounted ESS.

set to be 2 cm for effective EP signal recording.[21] The FS is designed with a 1/5 ribbon width to arc radius ratio in order to balance the trade-off between stretchability and occupied area, according to our recent mechanics of serpentine research.[22] The same FS design is not applicable to the stretchable Al coil because it will consume too much space when many turns are needed for higher inductance. Therefore a double-stranded serpentine design is proposed (Figure 2a), which saves space without compromising the number of turns or the stretchability too much. The two longhorns at the upper left and right corners of the Au pattern serve as alignment markers for printing Au and Al devices on the same tape. The overall size of the device area is 7.5 cm × 5 cm. Detailed quality examination of "cut-and-paste" manufactured specimens is provided in Supporting Information Figures S2–S4.

The Young's moduli of the different materials used in ESS and ESS itself are measured by uniaxial tension tests using an RSA-G2 dynamic mechanical analyzer (TA Instruments) and summarized in Supporting Information Figure S5 and Supporting Information Table S1. Out of all substrate materials that have been tested, including tattoo paper, Tegaderm, and KRST, Tegaderm is the most compliant one. It's modulus (7.4 MPa) is close to the high end of the modulus of human skin (0.32–4 MPa[23]) Supporting Information Figure S5c shows that Tegaderm is composed of a backing layer and an adhesive layer. Using a scotch tape to peel the adhesive layer off the backing layer, we measured the stress–strain curves of each layer as shown in Supporting Information Figure S5d.

The stretchability of different serpentine ribbons on Tegaderm tapes was tested using a customized tensile tester with in situ resistance measurement and top down webcam observation (Figure 2b, left panel).[24] When electrical resistance is measured as a function of the applied uniaxial tensile strain, the applied strain at which the resistance explodes (e.g., $R/R_0 = 1.1$) is considered the strain-to-rupture or stretchability.[19] According to Figure 2b, right panel, while straight Al-on-PET and Au-on-PET ribbons exhibit limited stretchability (2.89% and 13.72%, respectively), their serpentine-shaped ribbons as shown in Supporting Information Figure S6a (Al coil), S6b (Au EP electrode), and S6c (Au RTD) are much more stretchable, well beyond the elastic limit of human skin (30%).[25] For serpentine ribbons such as the Al coil and Au RTD, rupture sites are always found at the crest of the arc (Supporting Information Figure S6a,c), whereas for serpentine network such as the Au EP electrode, fracture occurs first at ribbon intersections (Supporting Information Figure S6b) due to strain concentration and overcutting at turning points (Supporting Information Figure S4d–i). Cycleability of the Au serpentine was tested on an RSA-G2 dynamic mechanical analyzer (TA Instruments) with a frequency of 2 Hz. Supporting Information Figure S7 displays the resistance change of the Au serpentine as a function of the number of cycles. When applied strain is 20%, the

Au serpentine can be stretched 10 000 times before the resistance increases by 1%.

Supporting Information Figure S8 displays ESS on three different types of substrates and how they can be applied to human skin. While Tegaderm and tattoo papers are thin, transparent, and truly skin-like (Supporting Information Figure S8a–h), the KRST is much thicker and behaves like a cloth tape (Supporting Information Figure S8i–l). Because of the thickness, KRST does not crumple after being peeled off from the skin and the silicone adhesive allows multiple attachment and detachment before losing adhesion. Skin–ESS interaction is shown in Figure 2c and more in Supporting Information Figure S9, which validates the tattoo-like mechanics of the ESS. The electrical resistance of the Al and Au serpentines before and after various kinds of skin deformation (stretching, compression, shear, poking, etc.) is provided in Figure 2d. It is evident that the ESS can survive all possible skin deformations without any mechanical degradation.

The multiparametric ESS has been successfully applied to perform continuous EP, skin temperature, and skin hydration measurements. EP signals on the surface of human skin measure the flow of ions in the underneath tissues and organs, which reflects their health and function. For example, noninvasive ambulatory monitoring of ECG on human chest can help detect multiple important features of heart malfunction like irregular heartbeat (arrhythmia).[26] EMG reflects human muscle activity and can identify neuromuscular diseases and serve as a control signal for prosthetic devices or other machines.[21] EEG measured from the surface of human scalp can be used to not only capture cognitive and memory performance[27] but also chart brain disorders like epilepsy[28] and stroke.[29] **Figure 3**a displays ECG measurement from human chest using silver/silver chloride (Ag/AgCl) gel electrodes and the ESS without applying any conductive gels. Both ESS and Ag/AgCl electrodes were connected to a small portable amplifier (AvatarEEG) with a shared ground port through a homemade reusable connector (Supporting Information Figure S10). Out of the three EP electrodes integrated on the ESS, the center one is utilized as a ground and the other two electrodes measure EP signals in a bipolar montage to reflect the difference in electrical potential. Signals recorded by AvatarEEG were processed using a Principle Component Analysis based algorithm,[30] with the final results shown in Figure 3a. It is evident that the important features of ECG are captured by both electrodes, but the ECG measured by our ESS demonstrates higher amplitude. We also placed the same type of ESS over the forearm, specifically on the flexor muscles, to measure the EMG during two hand clenches (Figure 3b). The intensity of the gripping force can be measured by a commercial dynamometer (Exacta) and it is clear that the higher gripping force corresponds to higher signal amplitude in the EMG. Finally, we measured EEG by adhering Ag/AgCl electrodes and the ESS on human forehead. Both electrodes were referenced against one FS electrode placed behind the human

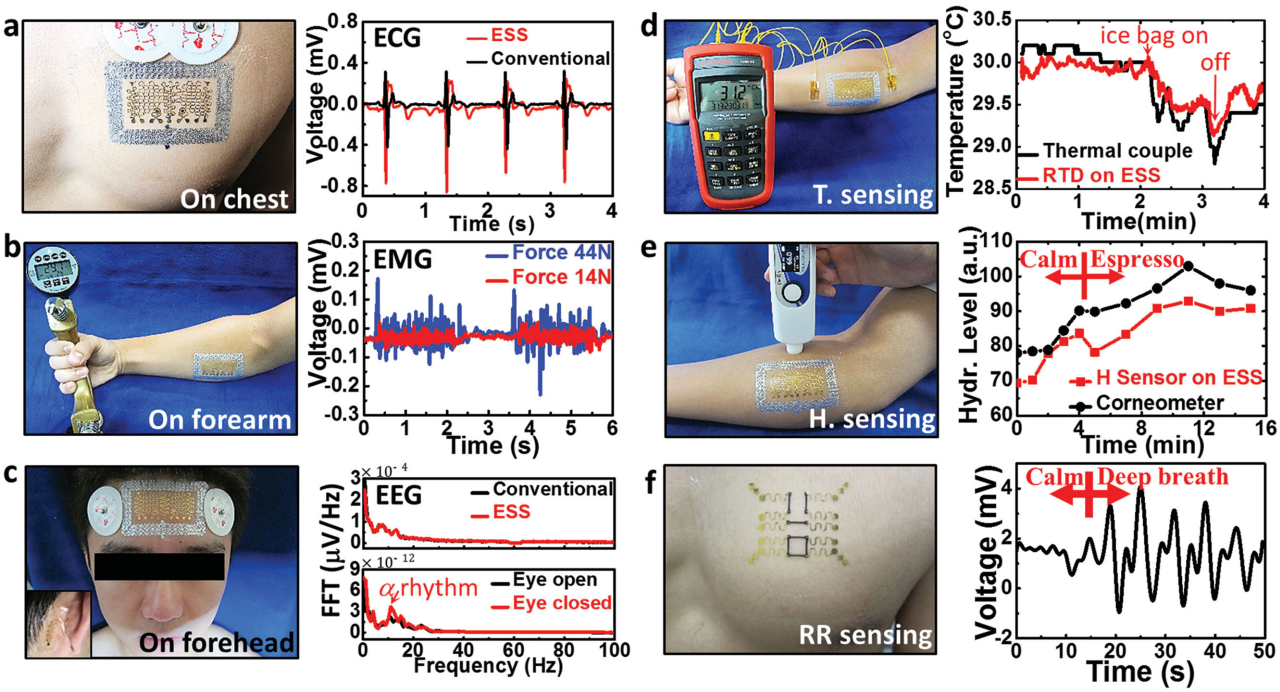

Figure 3. ECG, EMG, EEG, skin temperature, skin hydration, and respiratory rate measurements by ESS. a) ECG simultaneously measured by ESS (red) and Ag/AgCl electrodes (black). Stronger ECG signals were obtained by the ESS. b) ESS attached on human forearm for EMG measurement when the subject is gripping a commercial dynamometer with different forces. EMG of higher amplitude (blue) corresponds to higher gripping force. c) EEG measured on human forehead by both ESS (red) and Ag/AgCl electrodes (black). Two frequency spectra of the EEG are well overlapped. 10 Hz alpha rhythm measured by ESS is clearly visible when eyes were closed. d) Skin temperature change measured by epidermal RTD (red) and thermocouple (black) found good correlation. e) Real time skin hydration before and after Espresso intake measured by both commercial coaxial corneometer (black) and ESS (red). f) Voltage outputs from the electrically conductive rubber (ECR) Wheatstone bridge during normal and deep breath.

Adv. Mater. **2015**,
DOI: 10.1002/adma.201502386

ear (on the mastoid), as shown in Figure 3c, left panel. Signals were high and low passed filtered at 0.1 and 40 Hz, respectively. Frequency spectra were calculated using standard fast Fourier transformations (FFTs). The remarkable agreement between conventional and ESS measured EEG is evident in Supporting Information Figure S11. Their FFT spectra almost fully overlap in the upper right panel of Figure 3c, which confirms that conventional and ESS electrodes are almost indistinguishable in measuring EEG signals, but the ESS offers additional merits including conformability, softness, and customizable electrode patterns. The lower right panel of Figure 3c compares the FFT of the ESS measured EEG while the subject's eyes were staying open (black) or closed (red). One can note the expected increase in relative alpha power whiles the subject's eyes were closed (centered around 10 Hz).

In addition to EP, skin temperature, skin hydration, and skin deformation are also useful indicators of human physiology. For example, skin temperature is associated with cardiovascular health, cognitive state, and tumor malignancy.[31–33] Skin hydration is widely used in dermatology and cosmetology for the detection of diseases (e.g., eczema, atopic dermatitis, etc.),[34,35] the assessment of mental stress or hormone levels,[36,37] and the evaluation of medical therapies or cosmetic treatments.[38,30] Quantifying skin deformation is useful for the detection of gesture,[39] respiration, as well as motion disorders.[16] Ultrathin, stretchable RTD can be built as a narrow but long ribbon of Au FS as labeled in Figure 2a, which has a high initial resistance R_0 and a predictable change in resistance as the temperature changes. RTD calibration is provided in Supporting Information Figure S12a,b. Strain effect on RTD reading is also investigated. Supporting Information Figure S12c shows that when the RTD is subjected to a tensile strain of 25% (i.e., the elastic limit of skin), the resistance change is within 0.15%, which corresponds to less than 1 °C temperature change. This finding suggests that temperature measurement should be performed under minimal skin deformation. To perform skin temperature measurement, the epidermal RTD was attached on human forearm, along with a commercial thermocouple (TMD-56, Amprobe) as pictured in Figure 3d, left panel. Skin temperature measured by the epidermal RTD (red) and the thermocouple (black) are plotted in Figure 3d, right panel. Skin temperature was initially stabilized at around 30 °C. At t = 2′13″, an ice bag was brought in contact with the RTD and skin for 1 min and then removed. The corresponding temperature drop and recovery are clearly visible in the graph of Figure 3d. The strong correlation between RTD and thermocouple outputs has validated the use of RTD as a soft and stretchable skin temperature detector.

Skin hydration level is reflected by the impedance of skin,[11] which is conveniently measured by impedance sensors in the coaxial dot-ring design as labeled in Figure 2a. Laminating the epidermal hydration sensor (H. sensor) on human skin, an inductance, capacitance, and resistance (LCR) meter (Digital Multimeter, Rigol) was used to measure the impedance at different frequencies as well as different skin hydration levels. A commercial corneometer (MoistureMeterSC Compact, Delfin Inc.) was used to quantify the skin hydration level. Hydration sensor calibration is provided in Supporting Information Figure S13a,b. Figure 3e illustrates a continuous hydration measurement with both epidermal H. sensor and the corneometer before and after the subject drank a can of cold Espresso. The caffeine in Espresso is expected to lead to perspiration as it stimulates human central nervous system, which activates the sweat glands. The results are shown in Figure 3e, right panel, which clearly indicates gradual increase of hydration after drinking Espresso based on the measurements of both the epidermal H. sensor and the corneometer. The initial increase in hydration before drinking Espresso is believed to be caused by the ESS lamination which is discussed in detail in Supporting Information Figure S14. It is also interesting to note that skin hydration peaked 7 min after drinking the Espresso and started to decay after that, likely due to the thermoregulation of the body. An artifact of contact pressure in measuring skin hydration with ESS was noticed and can be prevented as discussed in Supporting Information Figure S15.

Epidermal respiratory rate sensor was build using electrically conductive rubber (ECR), which is similar to our previous soft strain gauge work,[40] but is made by the more cost and time effective "cut-and-paste" method. Unlike conventional microfabrication techniques that are limited to inorganic materials, the "cut-and-paste" process developed here can be applied to a much broader category of materials, including elastomeric sheets. As a demonstration, we fabricated stretchable strain gauges employing ECR (Elastosil LR 3162, Wacker Silicones) as the strain-sensitive resistor, and Au-on-PET serpentine ribbons as the stretchable interconnects (see Supporting Information Figure S16 for details). Sensor validation was performed by applying Tegaderm-supported ECR-based strain gauges on the chest of a human subject (Figure 3f, left picture) and various respirational patterns were measured. Figure 3f, right graph, illustrates the deformation of human chest during normal breath and deep breath using the Wheatstone bridge. Larger amplitude and lower frequency are observed for deep breath.

Compared with silicon nanomembrane[39,41] and ECR[40] based skin-integrated stretchable strain gauges, epidermal strain sensors based on planar stretchable capacitor can operate wirelessly.[13] Instead of using stretchable capacitor, here we explore planar stretchable inductors to build wireless epidermal strain sensors. The double-stranded serpentine design of the planar inductor coil as depicted in Figure 2a has taken into account overall size, stretchability, overall inductance, and strain sensitivity (see Supporting Information). **Figure 4** illustrates the wireless measurement on the sensor coil. A circular reader coil is connected to an Impedance Analyzer (HP 4194A) via a standard BNC-RCA adaptor. The reader coil is inductively coupled to the sensor coil in a transformer like configuration (Figure 4a). The experimental setup is given in Figure 4b and there was no cable connection between the reader and the sensor coil. By measuring the impedance response of the coupled circuit as a function of frequency, the resonance frequency can be determined as the dip in the phase–frequency curve (see details in Supporting Information).

We performed uniaxial stretch tests on Tegaderm supported stretchable coils (Figure 4c) and recorded strain-induced shift of resonance frequency of the coupled circuit, as shown in Figure 4d. Measured resonance frequency as a function of applied strain is plotted in red in Figure 4e, which shows a monotonic decay as the sensor coil is uniaxially elongated. The

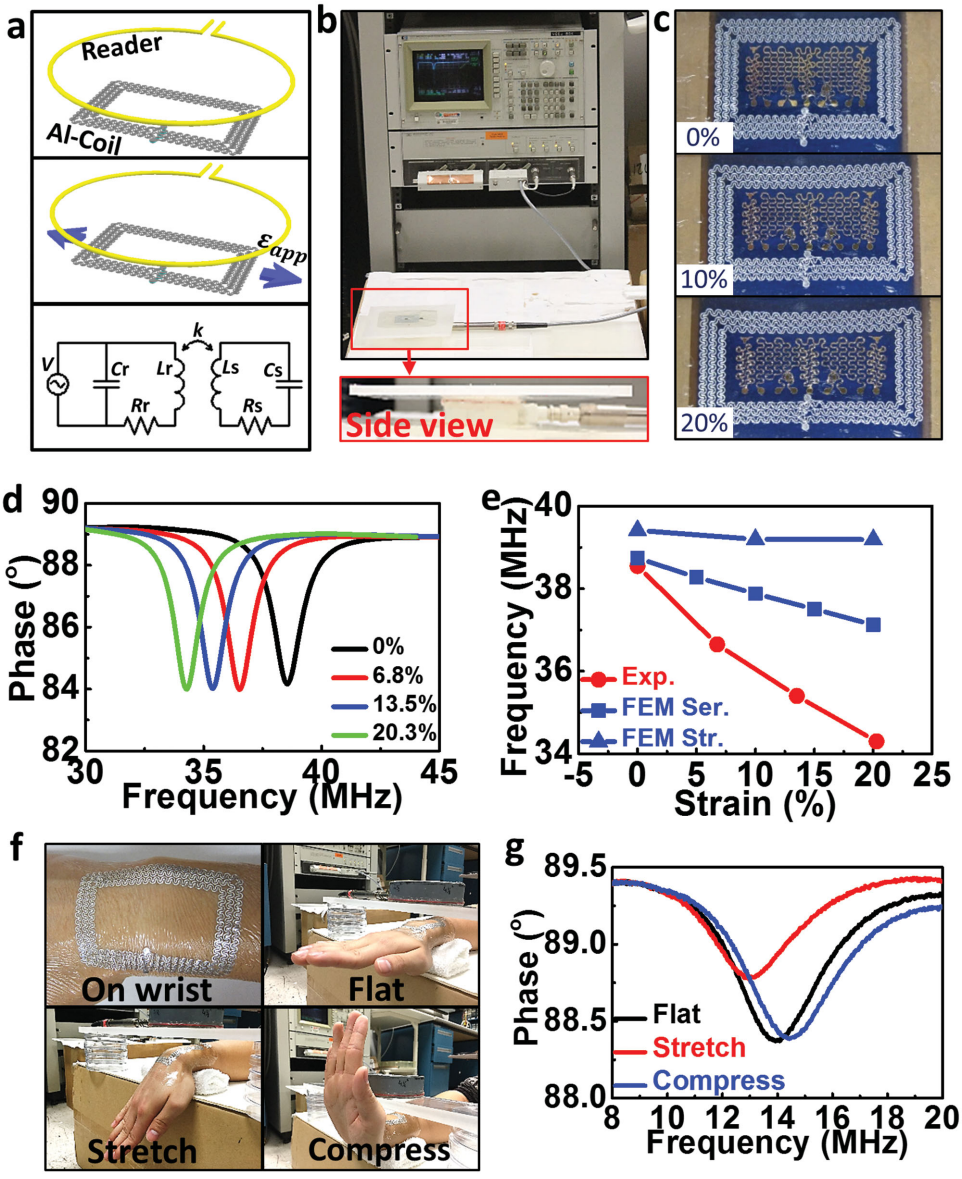

Figure 4. Wireless epidermal strain sensor based on stretchable Al coil. a) Schematics of the wirelessly coupled reader and sensor coils. b) Experimental setup for the measurement of the resonance frequency of the coupled system. The sensor coil was place on top of the reader coil and separated by a 6 mm thick acrylic slab plus 4 mm air gap. The reader was connected to an Impedance Analyzer (HP 4194A). c) Images of the sensor coil stretched horizontally by 0%, 10%, and 20%, respectively. d) Phase response of the coupled system as a function of sweeping frequency at different applied strains. e) Both experimental (red) and FEM (blue) results showing decreased resonance frequency with increased tensile strain. f) Sensor coil attached on human wrist (top left) under different hand gestures: "flat" (top right), "stretch" (bottom left), and "compress" (bottom right). g) Resonance frequency decreases when the sensor coil is stretched by the wrist, and increases when compressed by the wrist.

resonance frequency shifted from 38.6 MHz in the undeformed shape down to 34.3 MHz at the strain of 20%, which is more sensitive to deformation compared to a previously reported stretchable epidermal antenna.[17]

FEM analysis on stretchable coils has been carried out through a combination of ABAQUS standard and ANSYS Maxwell package (see Supporting Information Figure S18 for details) and the results are plotted in blue in Figure 4e, with squares representing serpentine coils (Supporting Information Figure S19a,b) and triangles representing straight coils (Supporting Information Figure S19c,d). Comparing the two results, straight coil appears less sensitive to applied strain, which is undesirable for strain sensing application but could be advantageous for antenna application when stable resonance frequency is needed. Analytical modeling of single and multiturn straight coils is given in Supporting Information Figure S20. All results (experimental, numerical, and analytical) suggest a decay of resonance frequency with increasing uniaxial tensile strain, but the discrepancy between experimental and FEM results requires future studies.

The effect of reader-sensor distance has also been investigated (Supporting Information Figure S21a,b). It is evident

Adv. Mater. **2015**,
DOI: 10.1002/adma.201502386

that the resonance frequency does not depend on the distance whereas the phase dip does. Specifically, the smaller the gap, the larger the phase dip, thus the higher coupling factor (*k* factor as labeled in Figure 4a bottom frame). One way to improve the coupling factor and hence enlarge the sensing distance is to increase the overall size of either the reader or the sensor coil, with a tradeoff of course in the wearability of the sensor and the portability of the reader.

Skin deformation measurement was performed by attaching the sensor coil on the dorsal wrist and bringing the reader coil within 45 mm distance from the sensor coil. Three layers of tattoo paper (Silhouette) were applied between the sensor coil and the skin to compensate for capacitive loading induced by the skin. Three wrist gestures "flat," "stretch," and "compress" were measured (Figure 4f). Phase measurement for the three gestures is plotted in Figure 4g, which reveals several interesting findings. First, the resonance frequency drops from 38.6 to 13.92 MHz before and after the sensor coil was applied on the skin, which is due to the substantial capacitive loading induced by the skin.[42] The second observation is that "stretch" reduces the resonance frequency (from 13.92 to 12.99 MHz) whereas "compress" slightly increases resonance frequency (from 13.92 to 14.41 MHz), as expected. Repeatability test was conducted by forming the wrist gestures in the sequence "flat," "stretch," and "compress" twice and the result (Supporting Information Figure S21c,d) shows that the wireless strain gauge coil can offer very repeatable measurements of joint bending.

The planar stretchable coil also has the potential to work as an NFC antenna for transferring signals measured by the ESS wirelessly to a remote receiver.[17] In order to transfer data properly, the resonance frequency should remain as steady as possible during the transferring process. We therefore tested the coil response when it is placed on human chest and the subject was under deep inhalation and exhalation. Supporting Information Figure S21e,f indicates that the resonance frequency only changed from 13.06 to 12.80 MHz, for either deep inhalation or exhalation. The insensitivity of resonance frequency to chest deformation associated inhalation and exhalation makes it possible to be used as a stable epidermal antenna for chest ESS.

In conclusion, we have demonstrated a versatile, cost- and time-effective method to manufacture multimaterial, multiparametric ESS that can be intimately but noninvasively and unobstructively applied on human skin to measure ECG, EMG, EEG, skin temperature, skin hydration, respiratory rate, and joint bending. The "cut-and-paste" method enables completely dry, benchtop, freeform, and portable manufacture of ESS within minutes, without using any vacuum facilities or chemicals. The "cut-and-paste" method has proved effective in patterning metal-on-polymer laminates and elastomeric sheets, but it is not applicable to ceramic-coated polymer as indentation of the cutting blade would easily fracture intrinsically brittle ceramic film. However, we have demonstrated a variation of the "cut-and-paste" method to manufacture highly stretchable transparent interconnects based on brittle indium tin oxide film.[24] In addition to ESS, the "cut-and-paste" manufacturing method is expected to be useful for the manufacture of other stretchable devices including stretchable circuit boards which house rigid IC chips[43] and deployable structure health monitoring sensor networks.[44]

Experimental Section

Fabrication of ECR-Based Stretchable Strain Gauges: The ECR-based stretchable strain gauge was made by a two-step "cut-and-paste" process. The ECR is a clayish, two-component compound which requires thermal curing. The A and B components were first fully mixed by a drill mixer in a 1:1 ratio in weight and then squeezed by two parallel acrylic slabs pressured by binder clips. The squeezed ECR compound along with the acrylic slab and binder clips was then put into an oven in 70 °C for 4 h. After curing, an ECR film was obtained and the thickness of the ECR film turned out to be 120–140 μm. The ECR film was then cut and pasted onto Tegaderm to form the resistor and Wheatstone bridge. The Au-on-PET foil was then cut and pasted onto the same Tegaderm guided by alignment markers to form the serpentine interconnects of the strain gauges.

Measurement and Processing of EEG: For EP measurements, conventional and ESS channels were amplified using the AvatarEEG system in 24 bit DC mode at an initial sampling rate of 500 Hz. EEG signals were recorded with respect to the mastoid reference channel across a 297 s recording epoch. Offline, the data were then bandpass-filtered between 0.1 and 40 Hz and then visually inspected for artifacts and blinks. Contaminated sections were removed from the analysis. Artifact-free EEG data were then divided into two conditions: a 52 s epoch of resting eyes opened and a 52 s epoch of resting eyes closed. Spectral power measures were computed for each condition via FFT with a Hamming window.

Experiments on Human Subjects: Informed signed consent was obtained from all human test participants.

Supporting Information

Supporting Information is available from the Wiley Online Library or from the author.

Acknowledgements

S.Y., Y.-C.C., L.N., P.P., B.S., R.Y., N.L., D.N., and D.S. conducted device design, fabrication, calibration, and testing. S.Y. led the FEM analysis with the assistance of J.S. D.S. Y.C., P.W., S.Y., Y.-C.C., L.N., and R.Y. served as human subjects. L.N. and D.S. performed EP analysis. N.L., D.N., and D.S. supervised and coordinated the project. N.L., S.Y., Y.-C.C., L.N., P.P., D.N., and D.S. wrote the paper. This work is based upon work supported in part by the National Science Foundation under Grant Nos. CMMI-1301335 and CMMI-1351875 (CAREER). N.L. acknowledges the 3M Non-Tenured Faculty Award. Any opinions, findings, and conclusions or recommendations expressed in this material are those of the authors and do not necessarily reflect the views of the National Science Foundation nor 3M.

Received: May 19, 2015
Revised: August 5, 2015
Published online:

[1] N. Bowden, S. Brittain, A. G. Evans, J. W. Hutchinson, G. M. Whitesides, *Nature* **1998**, *393*, 146.
[2] J. R. Ives, S. M. Mirsattari, D. Jones, *Clin. Neurophysiol.* **2007**, *118*, 1633.
[3] G. Schwartz, B. C. K. Tee, J. G. Mei, A. L. Appleton, D. H. Kim, H. L. Wang, Z. N. Bao, *Nat. Commun.* **2013**, *4*, 1859.
[4] S. Gong, W. Schwalb, Y. W. Wang, Y. Chen, Y. Tang, J. Si, B. Shirinzadeh, W. L. Cheng, *Nat. Commun.* **2014**, *5*, 3132.
[5] S. Gong, D. T. H. Lai, B. Su, K. J. Si, Z. Ma, L. W. Yap, P. Guo, W. Cheng, *Adv. Electron. Mater.* **2015**, *1*, DOI: 10.1002/aelm.201400063.

[6] D. H. Kim, R. Ghaffari, N. S. Lu, J. A. Rogers, *Annu. Rev. Biomed. Eng.* **2012**, *14*, 113.
[7] D. H. Kim, N. L. Lu, R. Ghaffari, J. A. Rogers, *NPG Asia Mater.* **2012**, *4*, e15.
[8] D. H. Kim, N. S. Lu, R. Ma, Y. S. Kim, R. H. Kim, S. D. Wang, J. Wu, S. M. Won, H. Tao, A. Islam, K. J. Yu, T. I. Kim, R. Chowdhury, M. Ying, L. Z. Xu, M. Li, H. J. Chung, H. Keum, M. McCormick, P. Liu, Y. W. Zhang, F. G. Omenetto, Y. G. Huang, T. Coleman, J. A. Rogers, *Science* **2011**, *333*, 838.
[9] X. Feng, B. D. Yang, Y. M. Liu, Y. Wang, C. Dagdeviren, Z. J. Liu, A. Carlson, J. Y. Li, Y. G. Huang, J. A. Rogers, *ACS Nano* **2011**, *5*, 3326.
[10] Y. Hattori, L. Falgout, W. Lee, S. Y. Jung, E. Poon, J. W. Lee, I. Na, A. Geisler, D. Sadhwani, Y. H. Zhang, Y. W. Su, X. Q. Wang, Z. J. Liu, J. Xia, H. Y. Cheng, R. C. Webb, A. P. Bonifas, P. Won, J. W. Jeong, K. I. Jang, Y. M. Song, B. Nardone, M. Nodzenski, J. A. Fan, Y. G. Huang, D. P. West, A. S. Paller, M. Alam, W. H. Yeo, J. A. Rogers, *Adv. Healthcare Mater.* **2014**, *3*, 1597.
[11] X. Huang, W. H. Yeo, Y. H. Liu, J. A. Rogers, *Biointerphases* **2012**, *7*, 1.
[12] X. Huang, H. Cheng, K. Chen, Y. Zhang, Y. Zhang, Y. Liu, C. Zhu, S.-c. Ouyang, G.-W. Kong, C. Yu, Y. Huang, J. A. Rogers, *IEEE Trans. Biomed. Eng.* **2013**, *60*, 2848.
[13] N. Lu, D. H. Kim, *Soft Robotics* **2013**, *1*, 53.
[14] A. J. Bandodkar, D. Molinnus, O. Mirza, T. Guinovart, J. R. Windmiller, G. Valdes-Ramirez, F. J. Andrade, M. J. Schoning, J. Wang, *Biosens. Bioelectron.* **2014**, *54*, 603.
[15] X. Huang, Y. H. Liu, K. L. Chen, W. J. Shin, C. J. Lu, G. W. Kong, D. Patnaik, S. H. Lee, J. F. Cortes, J. A. Rogers, *Small* **2014**, *10*, 3083.
[16] D. Son, J. Lee, S. Qiao, R. Ghaffari, J. Kim, J. E. Lee, C. Song, S. J. Kim, D. J. Lee, S. W. Jun, S. Yang, M. Park, J. Shin, K. Do, M. Lee, K. Kang, C. S. Hwang, N. S. Lu, T. Hyeon, D. H. Kim, *Nat. Nanotechnol.* **2014**, *9*, 397.
[17] J. Kim, A. Banks, H. Cheng, Z. Xie, S. Xu, K.-I. Jang, J. W. Lee, Z. Liu, P. Gutruf, X. Huang, P. Wei, F. Liu, K. Li, M. Dalal, R. Ghaffari, X. Feng, Y. Huang, S. Gupta, U. Paik, J. A. Rogers, *Small* **2015**, *11*, 906.
[18] M. A. Pacheco, C. L. Marshall, *Energy Fuel* **1997**, *11*, 2.
[19] N. S. Lu, X. Wang, Z. Suo, J. Vlassak, *Appl. Phys. Lett.* **2007**, *91*, 221909.
[20] H. Seitz, S. Marlovits, I. Schwendenwein, E. Muller, V. Vecsei, *Biomaterials* **1998**, *19*, 189.
[21] J. W. Jeong, W. H. Yeo, A. Akhtar, J. J. S. Norton, Y. J. Kwack, S. Li, S. Y. Jung, Y. W . Su, W. Lee, J. Xia, H. Y. Cheng, Y. G. Huang, W. S. Choi, T. Bretl, J. A. Rogers, *Adv. Mater.* **2013**, *25*, 6839.
[22] T. Widlund, S. Yang, Y.-Y. Hsu, N. Lu, *Int. J. Solids Struct.* **2014**, *51*, 4026.
[23] F. M. Hendriks, *Universiteitsdrukkerij TU Eindhoven*, Eindhoven, The Netherlands **2005**.
[24] S. Yang, E. Ng, N. Lu, *Extreme Mech. Lett.* **2015**, *2*, 37.
[25] V. Arumugam, M. D. Naresh, R. Sanjeevi, *J. Biosci.* **1994**, *19*, 307.
[26] N. V. Thakor, Y. S. Zhu, *IEEE Trans. Biomed. Eng.* **1991**, *38*, 785.
[27] W. Klimesch, *Brain Res. Rev.* **1999**, *29*, 169.
[28] F. Rosenow, K. M. Klein, H. M. Hamer, *Expert Rev. Neurotherapeutics* **2015**, *15*, 425.
[29] K. G. Jordan, *J. Clin. Neurophysiol.* **2004**, *21*, 341.
[30] M. Boguniewicz, N. Nicol, K. Kelsay, D. Y. M. Leung, *Semin. Cutan. Med. Surg.* **2008**, *27*, 115.
[31] C. R. Wyss, G. l. Brengelm, J. M. Johnson, L. B. Rowell, M. Niederbe, *J. Appl. Physiol.* **1974**, *36*, 726.
[32] T. M. Makinen, L. A. Palinkas, D. L. Reeves, T. Paakkonen, H. Rintamaki, J. Leppaluoto, J. Hassi, *Physiol. Behav.* **2006**, *87*, 166.
[33] E. Y. K. Ng, *Int. J. Therm. Sci.* **2009**, *48*, 849.
[34] C. Blichmann, J. Serup, *Contact Dermatitis* **1987**, *16*, 155.
[35] K. L. E. Hon, K. Y. Wong, T. F. Leung, C. M. Chow, P. C. Ng, *Am. J. Clin. Dermatol.* **2008**, *9*, 45.
[36] P. G. Sator, J. B. Schmidt, T. Rabe, C. C. Zouboulis, *Exp. Dermatol.* **2004**, *13*, 36.
[37] B. W. Tran, A. D. P. Papoiu, C. V. Russoniello, H. Wang, T. S. Patel, Y. H. Chan, G. Yosipovitch, *Acta Derm. Venereol.* **2010**, *90*, 354.
[38] S. M. Kleiner, *J. Am. Diet Assoc.* **1999**, *99*, 200.
[39] M. Ying, A. P. Bonifas, N. S. Lu, Y. W. Su, R. Li, H. Y. Cheng, A. Ameen, Y. G. Huang, J. A. Rogers, *Nanotechnology* **2012**, *23*, 344004.
[40] R. Kandasamy, X. Q. Wang, A. S. Mujumdar, *Appl. Therm. Eng.* **2008**, *28*, 1047.
[41] D. H. Kim, R. Ghaffari, N. S. Lu, S. D. Wang, S. P. Lee, H. Keum, R. D'Angelo, L. Klinker, Y. W. Su, C. F. Lu, Y. S. Kim, A. Ameen, Y. H. Li, Y. H. Zhang, B. de Graff, Y. Y. Hsu, Z. J. Liu, J. Ruskin, L. Z. Xu, C. Lu, F. G. Omenetto, Y. G. Huang, M. Mansour, M. J. Slepian, J. A. Rogers, *Proc. Natl. Acad. Sci. USA* **2012**, *109*, 19910.
[42] E. Kinnen, *Med. Electron. Biological Eng.* **1965**, *3*, 67.
[43] S. Xu, Y. H. Zhang, L. Jia, K. E. Mathewson, K. I. Jang, J. Kim, H. R. Fu, X. Huang, P. Chava, R. H. Wang, S. Bhole, L. Z. Wang, Y. J. Na, Y. Guan, M. Flavin, Z. S. Han, Y. G. Huang, J. A. Rogers, *Science* **2014**, *344*, 70.
[44] G. Lanzara, N. Salowitz, Z. Q. Guo, F. K. Chang, *Adv. Mater.* **2010**, *22*, 4643.

Adv. Mater. **2015**,
DOI: 10.1002/adma.201502386

ADVANCED MATERIALS

Supporting Information

for *Adv. Mater.,* DOI: 10.1002/adma.201502386

"Cut-and-Paste" Manufacture of Multiparametric Epidermal Sensor Systems

*Shixuan Yang, Ying-Chen Chen, Luke Nicolini, Praveenkumar Pasupathy, Jacob Sacks, Su Becky, Russell Yang, Sanchez Daniel, Yao-Feng Chang, Pulin Wang, David Schnyer, Dean Neikirk, and Nanshu Lu**

Supporting Information

"Cut-and-Paste" Manufacture of Multiparametric Epidermal Sensor Systems (ESS)

Shixuan Yang[1], Ying-Chen Chen[1, 2], Luke Nicolini[1, 3], Praveenkumar Pasupathy[2], Jacob Sacks[1], Su Becky[1], Russell Yang[1], Sanchez, Daniel[1], Yao-Feng Chang[1, 2], Pulin Wang[1], David Schnyer[4], Dean Neikirk[2], Nanshu Lu[1, 3, 5*]

[1]Center for Mechanics of Solids, Structures and Materials, Department of Aerospace Engineering and Engineering Mechanics, [2]Department of Electrical and Computer Engineering, [3]Texas Materials Institute, [4]Department of Phycology, [5]Department of Biomedical Engineering, the University of Texas at Austin, Austin TX 78712, USA.

Keywords: wearable, flexible electronics, epidermal, vital sign monitor, freeform manufacture

* Corresponding author: nanshulu@utexas.edu, 512-471-4208, 210 E. 24th St, Austin, TX 78712

Resolution, uniformity, and roughness of "cut-and-paste" manufacture

Figure S2 shows the resolution test results, where the same pattern was cut with different ribbon widths, from 600 μm down to 50 μm. The raw material being cut in this test is 9-μm-thick Al on 12-μm-thick PET foil (NEPTAPE® by NEPTCO, Inc.). It is evident that the pattern can be successfully cut when ribbon width is set to 200 μm, even though the uniformity is compromised. When ribbon width is 100 μm or less, the pattern can no longer be preserved. For our devices, we always use 400-μm-wide ribbons to ensure pattern integrity and device functionality. Ribbon width uniformity test was done by measuring and summarizing the widths of many cross-width lines which are evenly spaced along the median line of the serpentine, as shown in Figure S3a. We used 25-μm-thick Kapton sheet (Dupont) for this study. The cutter is set to cut 400-μm-wide ribbons but Figure S3b indicates that ribbon width distribution is centered on 340 μm, with a standard deviation of 87 μm. Thickness profile of the cut ribbon was examined by profilometer (Dektak 6M stylus profilometer, vender, USA) at three different locations on one ribbon (Figure S3c). Cross-sectional profile in Figure S3d shows that the edge width is less than 30 μm and the surface of the ribbon is quite flat. Cutting quality is found to be highly dependent on the sharpness of the cutting blade (Figure S4a). The cutting blade can be worn (Figure S4b) or destroyed (Figure S4c), depending on the cutting time, raw material, and parameter settings in the Silhouette Studio software. Therefore, blade condition should be carefully examined before running any cutting job. Cutting jobs with different cutting parameters (see figure caption of Figure S4) were also performed with the results displayed in Figures S4d-i. It is concluded that the cutting thickness setting, thickness of the foil to be cut, and the blade condition are the most important factors for cutting quality control. After the parametric study we came up with a set cutting parameters, sharpness=5, cutting rate=2, thickness=1, that gives the best quality for the Kapton sheet that we were cutting. The close-up of representative spots of our ESS is shown in Figures S4j-l.

Young's Moduli of different materials

A Dynamic Mechanical Analyzer (RSA-G2, TA Instruments) was used to perform uniaxial tension tests to obtain the Young's moduli of different materials used in our ESS. Specimens were cut into rectangular strips with aspect ratio of 10:1 and were pulled along the longitudinal direction. Stress-strain curves are offered in Figure S5a. Five different specimens were tested for each material and the Young's Modulus was obtained as the averaged value in Figure S5b and the Table S1.

Table S1 List of measured Young's modulus of different materials used in ESS

Material	Thickness (μm)	Young's Modulus (GPa)
PET (Goodfellow)	13	4.59
Kapton (Dupont)	12.7	3.59
KRST (3M)	200	0.228
Tattoo adhesive (Silhouette)	22	0.042
ESS on Tegaderm	60	0.011
Tegaderm (3M)	47	0.007
ECR (Wacker)	120	0.003

As a popular substrate used in ESS, Tegaderm is composed of a backing layer and an adhesive layer (Figure S5c). Using a scotch tape to peel the adhesive layer off the backing layer, we measured the stress-strain curves of each layer as shown in Supporting Information Figure S5d.

Calibration of RTD and hydration sensors

RTD resistance and temperature changes are related through the following equation:

$$\frac{\Delta R}{R_0} = \alpha(T - T_0) \quad \text{(S1)}$$

where α = 0.0037 $^{\circ}C^{-1}$ is the temperature coefficient of resistance of bulk Au, independent of the thickness or the length of the resistor. The RTD is made of FS ribbons consisting of 100 nm thick Au film on 12.5 μm thick transparent PET, with overall length as large as 0.3 m as labeled in Figure 2a and initial resistance of 353 Ω at T_0 = 26 $^{\circ}$C. By placing our RTD and a commercial thermocouple (TMD-56, Amprobe) on the same hotplate (Figure S12a), we calibrated our RTD to have an α of 0.0017 $^{0}C^{-1}$ (Figure S12b), which is smaller than the temperature coefficient of resistance for bulk Au, largely attributed to the surface scattering in thin metal films [1]. With this calibration curve available, measurement of the RTD resistance can be converted to temperature measurement using Equation (S1). Strain effect on RTD reading is also investigated. Figure S12c shows that when the RTD is subjected to a tensile strain of 25% (i.e., the elastic limit of skin), the resistance change is within 0.15%, which corresponds to less than 1°C temperature change. Therefore, our RTD is strain sensitive and to achieve reliable temperature reading, skin deformation should be minimized.

To calibrate the epidermal hydration sensor, a commercial corneometer (MoistureMeterSC Compact, Delfin Inc.) was used to quantify the skin hydration level, which was tuned by applying body lotion on the skin. The magnitude of the impedance is plotted as a function of frequency at different hydration levels in Figure S13a and as a function of hydration level at different frequencies in Figure S13b. As expected [2], impedance drops as either frequency or hydration increases. Figure S13 also suggests that the sensitivity of impedance to hydration decreases as frequency increases, so the 10 kHz calibration curve was used to convert impedance to hydration for future measurement.

Sweating induced by ESS lamination

Laminating ESS on dry skin may induce slight sweating. After measuring the initial skin hydration level by commercial corneometer on human forearm, we laminated ESS dot-ring hydration sensor at the same spot. The results of five consecutive impedance measurements by ESS at four different initial hydration levels are given in Figure S14. As the impedance was measured by frequency sweep, each measurement took 34 seconds to finish and each figure in Figure S14 took us 170 seconds to finish the 5 tests. Immediately after ESS was applied on initially dry skin, the impedance gradually dropped as time went by (Figure S14a&b). However, when skin was initially moisturized by hand lotion, the impedance almost stayed unchanged with time (Figure S14c&d). The fact that dry skin "sweats" after ESS application is probably due to moisture accumulation on the skin surface as the ESS hinders skin surface sweat evaporation. But hand lotion can slow down sweat evaporation from embedded sweat glands to skin surface so the measured hydration did not change much within the measurement time.

Effect of contact pressure in measuring skin hydration

It is important to notice that the contact pressure significantly affects the measurement of skin impedance. Mishandling of the measuring process such as loose contact of the ESS to the skin can largely fail a measurement. This is why commercial corneometers are equipped with pressure sensors at the tip and only hydration readings achieved under specified pressure range is valid. Figure S15a&b shows the magnitude and phase of skin impedance responding to repeated gentle pressure applied on a loosely attached ESS. The impedance magnitude can be dropped by orders and the impedance phase angle can be reduced by about 20 degrees. To eliminate the pressure artifact, we firmly attached the ESS on skin by applying one time, 10 second long, hard press on the ESS right after it is applied to the skin. Figure S15c shows the difference of impedance magnitude of a loosely and a firmly attached ESS, where the firmly attached ESS affords a more stable impedance measurement. Calibration of firmly

attached ESS is shown in Figure S15d. Black dots are hydration levels measured by commercial corneometer and red circles are impedance measured by the hydration sensor on the ESS. It again reflects that skin impedance decreases as skin hydration increases.

Calibration and FEM of ECR-based epidermal respiratory rate sensor

Three types of ECR strain gauges are fabricated as shown in Figure S16a. The vertical and horizontal ECR strips are used to measure the vertical and horizontal tensile strains by measuring their change in resistance. Figure S16b gives the calibration of the Gauge Factor (*GF*), which is defined as

$$GF = \frac{\Delta R/R_0}{\varepsilon} \tag{S2}$$

Temperature induced resistance change can be compensated in a square-shaped Wheatstone bridge as shown in Figure 3f. The sensitivity of output voltage to applied uniaxial strain is given in Figure S16c. FEM results of strain distributions in the ECR resistors are offered in Figure S16d when a horizontal tensile strain of 5% is applied on the Tegaderm substrate.

Figure S16e shows a normal respiratory rate pattern measured by a horizontal ECR resistor, where each peak indicates an inhalation. A respiratory rate of 18 times per minute can be deduced from Figure S16e, which is consistent with the normal adult respiratory rate of 16 to 20 times per minute. Figure S16f shows chest skin deformation due to cough measured by the Wheatstone bridge and cough induced voltage output pattern is characterized by undulated plateau.

Analysis for stretchable sensor coil

The resonance frequency (*f*) of the sensor coil depends on its inductance (L_s) and capacitance (C_s) through the equation

$$f_s = \frac{1}{2\pi\sqrt{L_s C_s}} \quad \text{S3)}$$

As we hope to build a low frequency RLC coil that operates < 100 MHz for easier measurement and for future use as an NFC antenna that operates around 13.56 MHz, Equation (S3) suggests that the coil should have high inductance and capacitance. The capacitance of a parallel-plate capacitor is given by

$$C_s = \varepsilon \frac{A}{d} \quad \text{(S4)}$$

where ε denotes the absolute permittivity of the dielectric layer, A is the overlapped area of the parallel plates, and d is the thickness of the dielectric layer between the plates. Since the area of the cut-and-pasted parallel plate should not be too big out of stretchability concerns, and the dielectric layer is fixed to be 12-μm thick PET, there is an upper limit of the feasible capacitance if no rigid chip capacitors are included. Therefore a coil with large inductance is preferred. Inductance depends on the layout of the coil. For a planar coil, its inductance depends on the number of turns, shape of the turns, and the area that is enclosed by the coil [3, 4]. In general, the larger the area, the more turns, the higher the inductance, which conflicts with the need of building a wireless strain sensor that is reasonability small so that it can be properly fitted on the majority part of human body. Another design goal is to make it highly stretchable and compliant so that it doesn't mechanically load the skin. Last but not least, it is desirable to have highly strain-dependent inductance for high sensitivity measurement. With aforementioned constraints and goals, we exploited a double-stranded serpentine design shown as the blue coils in Figure 2a. This design helps maximize the use of limited real estate to fill in as many serpentine-shaped turns as possible. In the meanwhile it leaves reasonable gap between serpentines so that stretchability of the coil is ensured, which is evidenced by Figure 2c and Figure S17.

The coil is carved out of commercially available Al-on-PET sheet (NEPTAPE® by NEPTCO, Inc.) consisting of 9-μm-thick Al and 12-μm-thick blue-colored PET. Thick Al film is preferred as it reduces the total resistance (energy loss) of the RLC coil such that the quality factor

$$Q_0 = \frac{1}{R}\sqrt{\frac{L}{C}} \qquad \text{S5)}$$

is large, in which Q_0 is the quality factor at resonance frequency (ω_0). The total resistance of the coil was measured by a digital multimeter (UT58D, Uni-Trend Group Limited) to be R_s = 20 Ω. To close the RLC circuit, a short, second layer Al-on-PET serpentine ribbon was printed on top of the first layer coil to link the inner and outer terminals of the first layer coil by forming two identical parallel-plate capacitors connected in series, as labeled in Figure 2a. The capacitance of each capacitor (7.52 pF) is obtained by substituting $\varepsilon = 19.92 \times 10^{-12}$ F/m (absolute permittivity of PET [5]), A = 4.5 mm^2, and d = 12 μm into Equation (S4), and the total capacitance of the two capacitors connected in series is half of the individual capacitance, i.e. C_s = 3.76 pF. The inductance of the coil cannot be easily calculated, but can be wirelessly measured.

For an undeformed coil, with f = 38.6 MHz and C_s = 3.76 pF, the inductance is computed to be L_s = 4.52 μH using Equation (S3). With R_s = 20 Ω, Equation (S5) yields the estimated Q_0 of our sensor coil to be 54.8. Experimentally, Q_0 can also be obtained through

$$Q_0 = \frac{\omega_0}{\Delta\omega} \qquad \text{S6)}$$

where ω_0 is the resonance frequency and $\Delta\omega$ is the full-width-half-maximum (FWHM) bandwidth of the resonance. Using this definition, we obtained $Q_0 \approx 34$ graphically, from the frequency response data. The difference in the estimated and measured values of Q_0 could be due to dielectric losses from the substrates and minor errors in R, L and C measurements or calculation.

Analysis for coupled sensor-reader circuit

In our wireless strain sensor based on stretchable Al coil, the planar inductor (L_s) and capacitor (C_s) together with the inductor's parasitic resistance (R_s) forms an RLC resonant circuit, as illustrated in Figure 4a bottom frame right. The sensor coil was wirelessly read via magnetic coupling by a parallel reader coil which was connected to an Impedance/Gain-Phase Analyzer (HP4194A). The reader coil is a one turn inductor with a diameter of 10.25 cm constructed using 18AWG magnet wire. The reader coil inductor (L_r) has its own series parasitic resistance (R_r) and capacitance (C_r) which also forms an RLC circuit. Thus the reader and the sensor together form two coupled RLC resonant circuits with a coupling factor of k (Figure 4a bottom frame). The HP4194A is used to obtain the swept-frequency impedance response of the two coupled circuits. The sensor coil's resonance frequency is given by Equation (S3) and the reader's resonance frequency is

$$f_r = \frac{1}{2\pi\sqrt{L_r C_r}} \tag{S7}$$

The parasitic capacitance induced by connectors and adaptors which connect the reader coil to the HP4194A add to C_r and hence lower f_r. The baseline response is that of the reader coil:

$$Z_{in} = C_r || (R_r + j\omega L_r) \tag{S8}$$

where || represents parallel circuit combination, ω is the angular frequency in radians/sec, and Z_{in} is the complex input impedance as a function of frequency. When the sensor is present, the input impedance is given by

$$Z_{in} = C_r || \left(R_r + j\omega L_r + \frac{\omega^2 M^2}{\left(R_s + j\omega L_s + \frac{1}{j\omega C_s} \right)} \right) \tag{S9}$$

where M is the mutual inductance between the reader and sensor coils. The HP4194A measures both magnitude $|Z_{in}|$ in Ohms (Ω) and the Phase (θ) in degrees ($^\circ$). For this work, we use the phase response

to determine the resonance frequency. By design we have ensured that $f_s \ll f_r$ which affords reliable estimation of the sensor's resonance frequency without perturbation from the reader's resonance. Thus the baseline response corresponds to the phase of the reader coil $\approx 90^{\circ}$. When the sensor is coupled to the reader, we observe a dip in the phase baseline with the minima point corresponding to the sensors resonance frequency (f_s). The size (i.e. deviation from the baseline) of this dip is dependent on the distance and orientation between the reader and the sensor coils as a result of changing coupling factor *k*. However the frequency corresponding to the dip, i.e. f_s, is independent of these changes. Thus one can reliably estimate f_s from this coupled but wireless measurement.

Strain induced sensor coil inductance change simulated by FEM

FEM is performed to model the inductance change of the sensor coil (one layer coil) with applied uniaxial tension. The mechanical deformation was modeled by ABAQUS and the inductance was modeled by ANSYS Maxwell. In ABAQUS, the sensor coil was modeled as Tegaderm-bonded serpentine-shaped wires with rectangular cross-sections and the entire structure was subjected to horizontal tensile displacement. Deformed coils were imported into ANSYS Maxwell and a 3D model was generated with rectangular cross-section 9 μm × 400 μm assigned to the coil. The coil was immersed in a rectangular box of atmosphere of size: 500 mm × 500 mm × 750 mm, to account for the dielectric effect of the surrounding air. Two extension wires were used to lead the two ports of the coil to the boundary of the atmospheric box (Figure S18a, atmosphere box not showing) and a current excitation of 1 A was applied across the ports. Solution Type of Magnetostatic was selected and the magnetic flux density fields (B field) of the deformed coils are given in Figure S18b-g. Coil inductance was a direct output of the result. Once numerical solutions of the sensor coil inductance were available, assuming capacitance unaffected by stretch, we were able to calculate the resonance frequency of the

stretched sensor using Equation (S3). This result is plotted in Figure 4e as blue, square markers. It is evident that our FEM results can predict the decrease of resonance frequency as a result of increasing inductance when the coil was uniaxially stretched. But there is still discrepancy between experimental and FEM results, which would require future investigation.

To reveal the effect of serpentine, we modeled the straight counterpart (Figure S19c) of the serpentine coil (Figure S19a), both bonded on Tegaderm substrates, subjected to the same tensile strains. The deformed shapes of the two coils after stretched by 30% are given in Supporting information Figure S19b&d. It is evident that the rectangular turns of the straight coil get distorted more than the serpentine coil, due to the high stiffness of the straight longitudinal edges. The resonance frequency results of straight coils are plotted in Figure 4e as the blue, triangle markers, which is almost stationary under stretch (39.4MHz for 0% and 39.2MHz for 30%). Therefore, serpentine coils are ideal for wireless skin strain sensing as it is both more deformable and more sensitive to strain. However, when applying those coils as NFC antenna, the fact that the resonance frequency of straight coils are less sensitive to mechanical strain compared with its serpentine counterpart poses a very interesting tradeoff between deformability and stability of frequency.

Theoretical analysis of straight single turn and multi-turn coils

Here we try to develop an analytical understanding of the inductance change with applied strain. The inductance of a planar, rectangular, single turn coil is approximately proportional to the square root of the area that is enclosed by the coil [6]

$$L \sim \sqrt{A} \sim \sqrt{l_1 l_2} \tag{S10}$$

where l_1 and l_2 are the initial length and width of rectangle, as labeled in Figure S20a.

Assuming the coil is bonded to a substrate with Poisson's ratio ν, when stretched by a strain of ε in direction 1, the deformed length and width becomes

$$l_{1(\varepsilon)} = (1+\varepsilon)l_1, \qquad l_{2(\varepsilon)} = (1-\nu\varepsilon)l_2 \tag{S11}$$

as labeled in Figure S20b.

Therefore the inductance of the deformed coil

$$L_{(\varepsilon)} \sim \sqrt{A_{(\varepsilon)}} \sim \sqrt{A(1+\varepsilon)(1-\nu\varepsilon)} \sim L_0\sqrt{(1+\varepsilon)(1-\nu\varepsilon)} \tag{S12}$$

And hence the strain dependence of the resonance frequency is given by

$$f_{(\varepsilon)} = \frac{1}{2\pi\sqrt{L_{(\varepsilon)}C}} \sim f_0 \frac{1}{[(1+\varepsilon)(1-\nu\varepsilon)]^{0.25}} \sim f_0\,(1+\frac{1}{4}(\nu-1)\varepsilon) \tag{S13}$$

which is plotted as a solid black curve in Figure S20e when $\nu = 0.5$ is assumed.

For a multi-turn planar rectangular coil as shown in Figure S20c, existing theory [3] has been extended to predict coil inductance under different applied strains. The inductance of a multi-turn rectangular coil is formulated as

$$L = \sum L_0 + \sum M \tag{S14}$$

where L is the total inductance, L_0 is the self-inductance of each straight segment and M is the mutual-inductance between any two segments.

The self-inductance is given by

$$L_0 = 0.002l\left[ln\left(\frac{2l}{GMD}\right) - 1.25 + \frac{AMD}{l} + \left(\frac{\mu}{4}\right)T\right] \tag{S15}$$

in which *GMD* is the geometric mean distance and *AMD* is the arithmetic mean distance, both depending on the coil geometry. l is the segment length, T is the frequency correction parameter which is taken to be 1 m/H and μ is the magnetic permeability and is also set to be 1 H/m.

The mutual-inductance is given by

$$M = 2lQ \tag{S16}$$

where Q is a parameter depending on the geometry of the segment

$$Q = ln\left\{\frac{1}{\beta} + \left(1 + \frac{1}{\beta^2}\right)^{0.5}\right\} - (1 + \beta^2)^{0.5} \quad \text{(S17)}$$

where $\beta = GMD/l$.

So given a rectangular coil with straight segment and uniform cross section, the total inductance of the coil solely depends on the layout of the coil, and the total inductance can be calculated in an iterative manner.[2]

Assuming the coil is deformed uniformly by longitudinal strain ε and transverse strain $-\nu\varepsilon$ as shown in Figure S20d, the frequency shift computed by Matlab using Equation (S13) is given as the dashed black curve in Figure S20e. It predicts a slightly lower resonance frequency of the undeformed linear coil than that measured for the undeformed serpentine coil. But the decay of resonance frequency with applied tensile strain is consistent with experimental and FEM results.

References for Supporting Information

[1] E. H. Sondheimer, Adv Phys 2001, 50, 499.

[2] X. Huang, W. H. Yeo, Y. H. Liu, J. A. Rogers, Biointerphases 2012, 7, 1.

[3] Greenhou.Hm, Ieee T Parts Hyb Pac 1974, Ph10, 101.

[4] S. W. Yoon, M. D. Glover, K. Shiozaki, Ieee T Power Electr 2013, 28, 2448.

[5] T. Nakamura, Y. Nikawa, Journal of Telecommunications and Information Technology 2001, 3, 66.

[6] S. S. Mohan, M. D. Hershenson, S. P. Boyd, T. H. Lee, Ieee J Solid-St Circ 1999, 34, 1419.

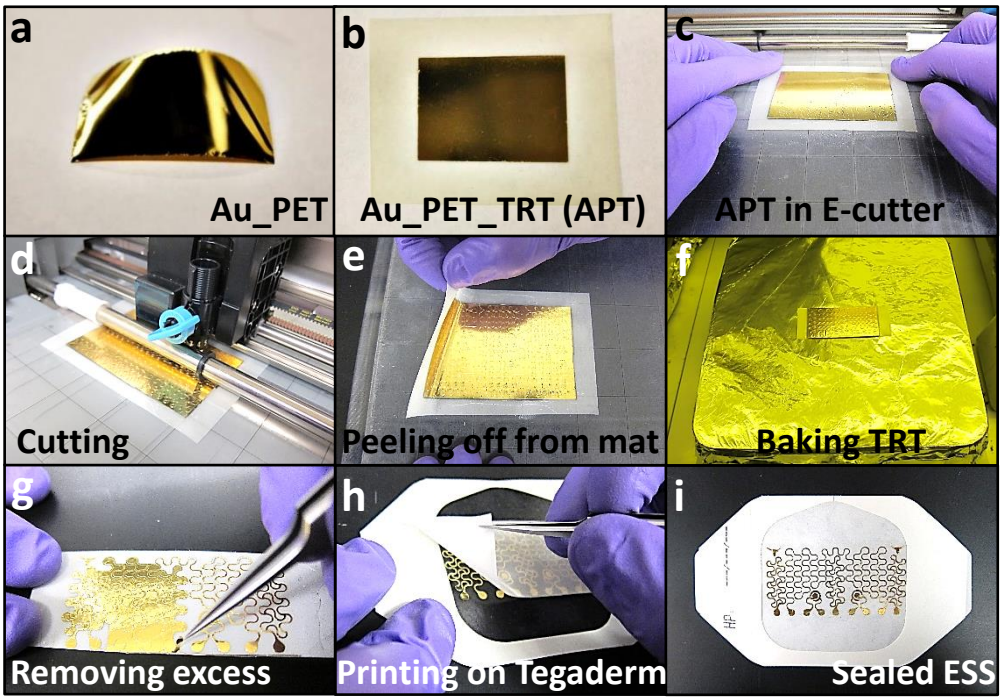

Figure S1: Pictures of the "cut-and-paste" process. (**a**) 100 nm Au coated 13-μm-thick transparent PET foil (Goodfellow USA). (**b**) Au-PET bonded onto TRT (APT) with the Au side touching TRT. (**c**) AP (Silhouette Cameo, USA). (**d**) Cutting machine carving seams in the Au-PET layer. (**e**) Peeling off cut APT layer from cutting mat. (**f**) Cut APT layer placed on hot plate to deactivate TRT adhesives. (**g**) Removing excessive Au-PET by tweezer. (**h**) Printing patterned Au-PET onto target substrate (in this case $2'3/8" \times 2'\,3/4"$ Tegaderm transparent dressing with liner removed). (**i**) As fabricated ESS on Tegaderm after putting back the liner. Patterned Au-PET is sandwiched between the transparent Tegaderm dressing and the white linear with Au touching the liner.

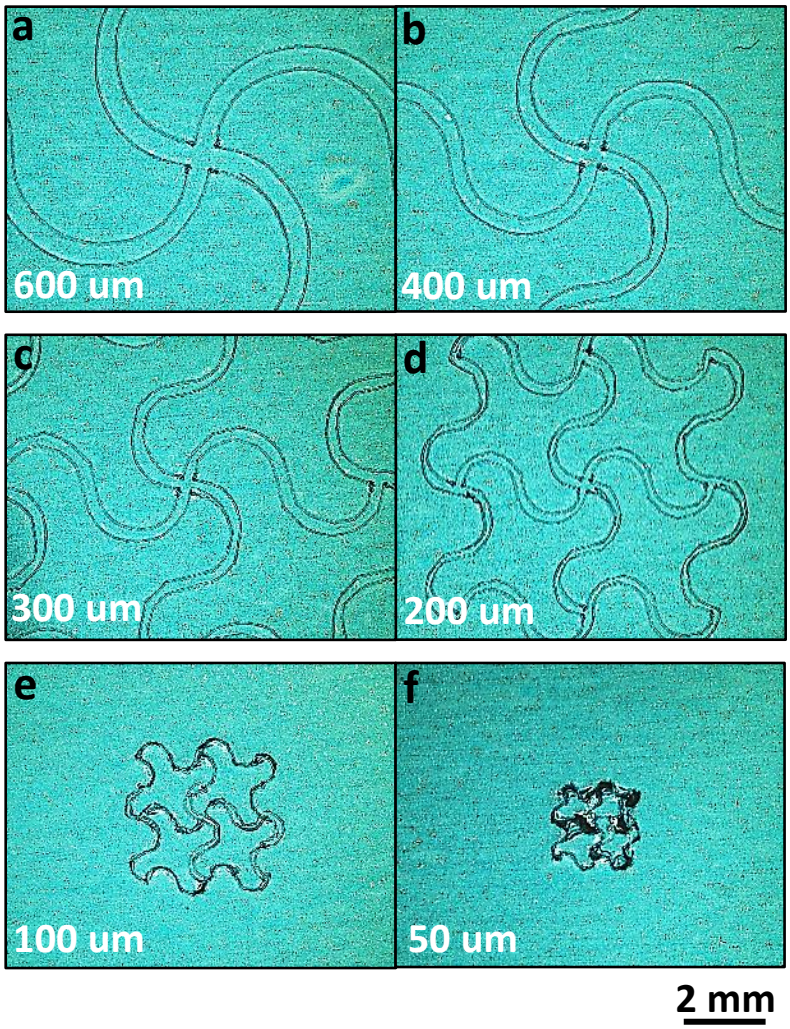

Figure S2: Resolution tests of the cutting machine. Pictures of the same seam pattern carved on blue PET-Al foil (Neptco Inc.) with different ribbon width: (**a**) 600 μm, (**b**) 400 μm, (**c**) 300 μm, (**d**) 200 μm, (**e**) 100 μm, and (**f**) 50 μm, by the cutting machine. The resolution of the cutting machine is determined to be 200 μm.

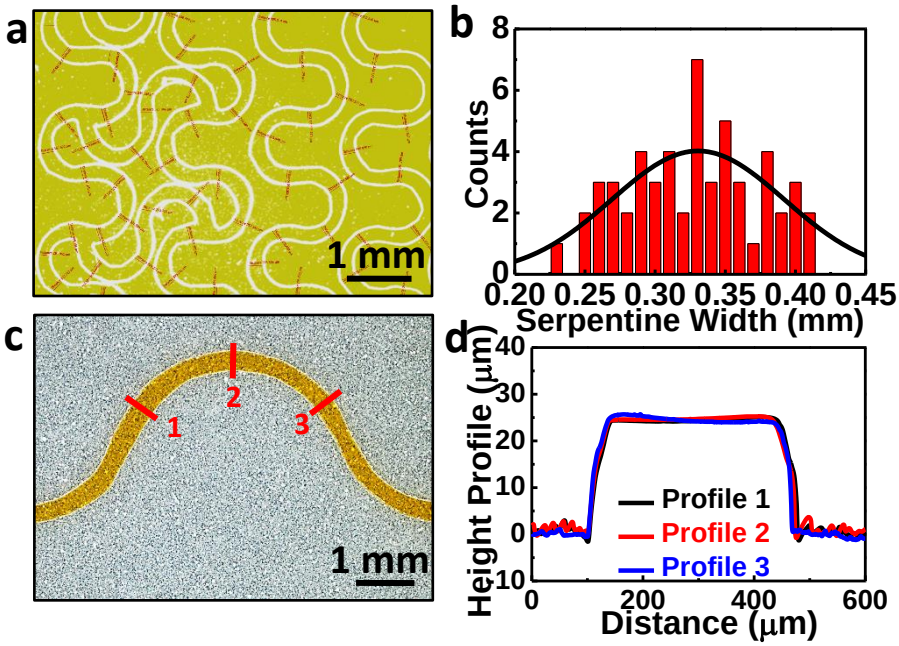

Figure S3: Width uniformity and surface profile of the cut ribbons. (**a**) Image of sampling spots for width uniformity investigation after cutting a 25 μm thick Kapton sheet on TRT. Ribbon width is 400 μm by drawing. (**b**) Width distribution fitted by Gaussian distribution (black curve) with a mean of 340 μm and a standard deviation of 87 μm. (**c**) Image of sampling spots for height profile investigation of the cut Kapton ribbon after excessive parts removed. (**d**) Height profile of the Katpon ribbon, showing flat plateau and steep transition zone.

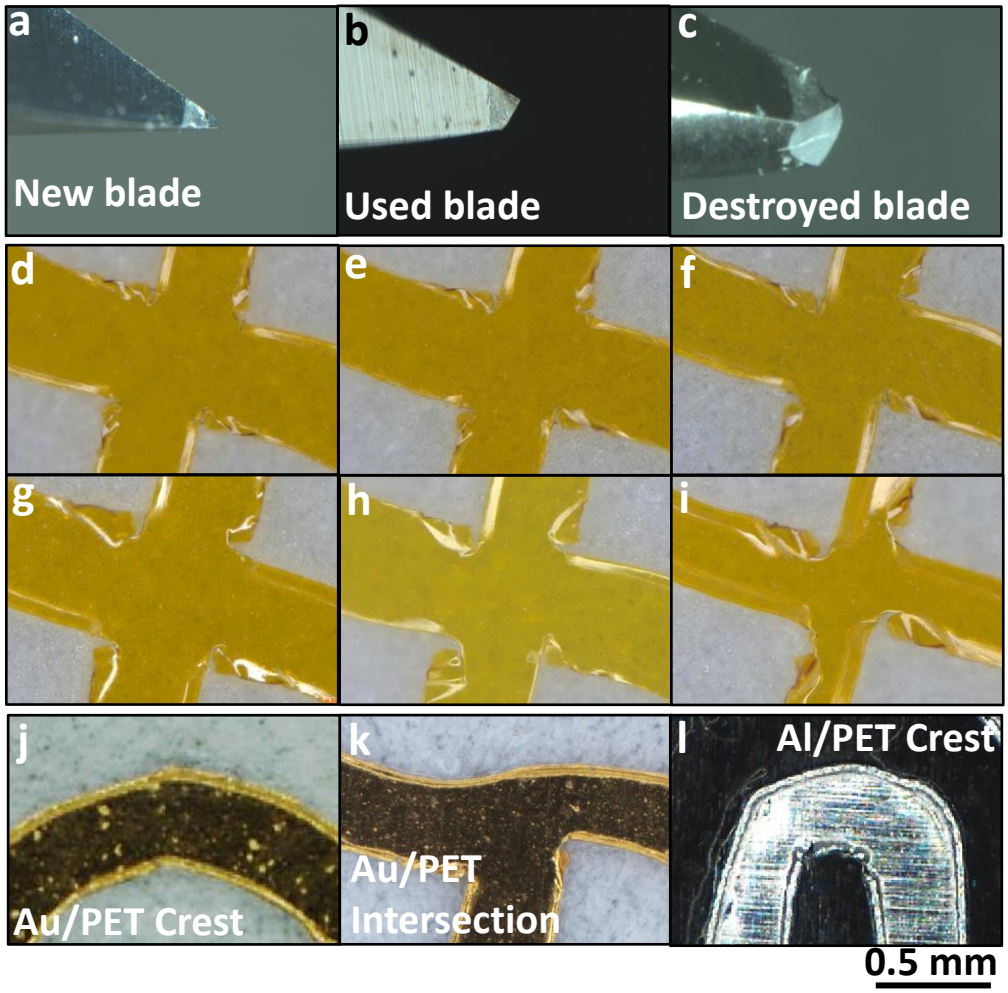

Figure S4: Effects of blade tip sharpness and cutting parameters. Images of a (**a**) new blade (**b**) a used blade and (**c**) a destroyed blade. Cutting results for different parameter combinations where KT stands for Kapton thickness, Sh for sharpness, Ra for cutting rate, Th for thickness, NB for new blade, UB for used blade: (**d**) KT=25.4μm, Sh=5, Ra=1, Th=7, NB (**e**) KT=25.4μm, Sh=10, Ra=1, Th=7, NB (**f**) KT=25.4μm, Sh=5, Ra=10, Th=7, NB (**g**) KT=25.4μm, Sh=5, Ra=1, Th=20 NB (**h**) KT=12.7μm, Sh=5, Ra=1, Th=7, NB (**i**) KT=25.4μm, Sh=10, Ra=1, Th=7, UB. Zoomed in images of final ESS cut by optimized parameters: (**j**) crest of the Au RTD, (**k**) intersection of the Au EP sensor, (**l**) crest of the stretchable Al coil.

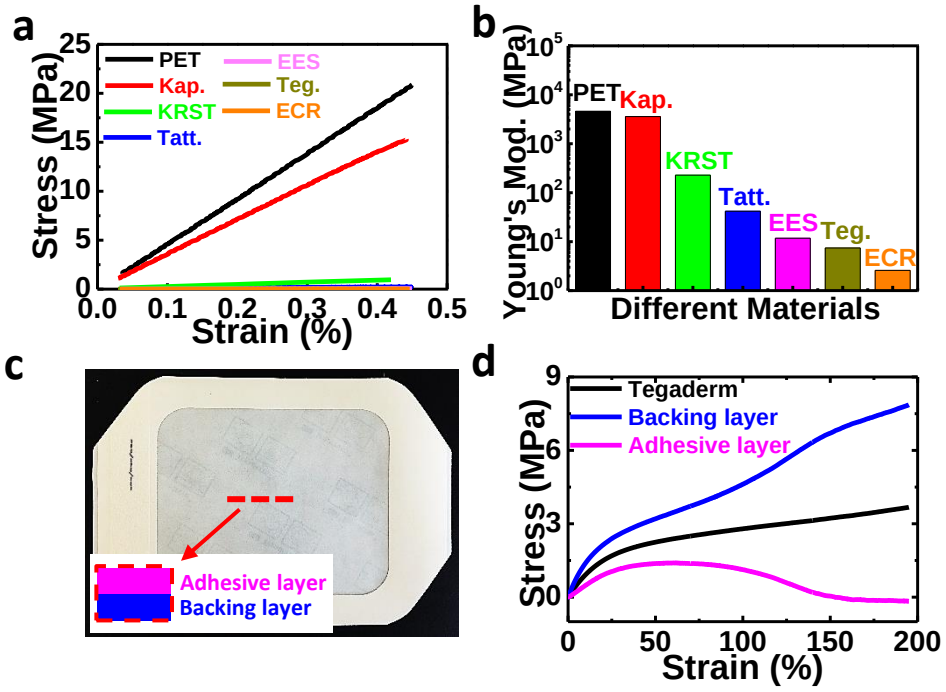

Figure S5: Stress-strain behavior of involved materials. (**a**) Uniaxial stress-strain curves of PET, Kapton, kind removal silicone tape (KRST), tattoo paper, ESS, Tegaderm, and ECR. (**b**) Bar plot of the Young's moduli in log scale. The thickness and modulus data is also given in Table S1. (**c**) Top view of Tegaderm, inset showing cross section of Tegaderm. (**d**) Uniaxial stress-strain curves of Tegaderm, Tegadmer backing layer and Tegaderm adhesive layer.

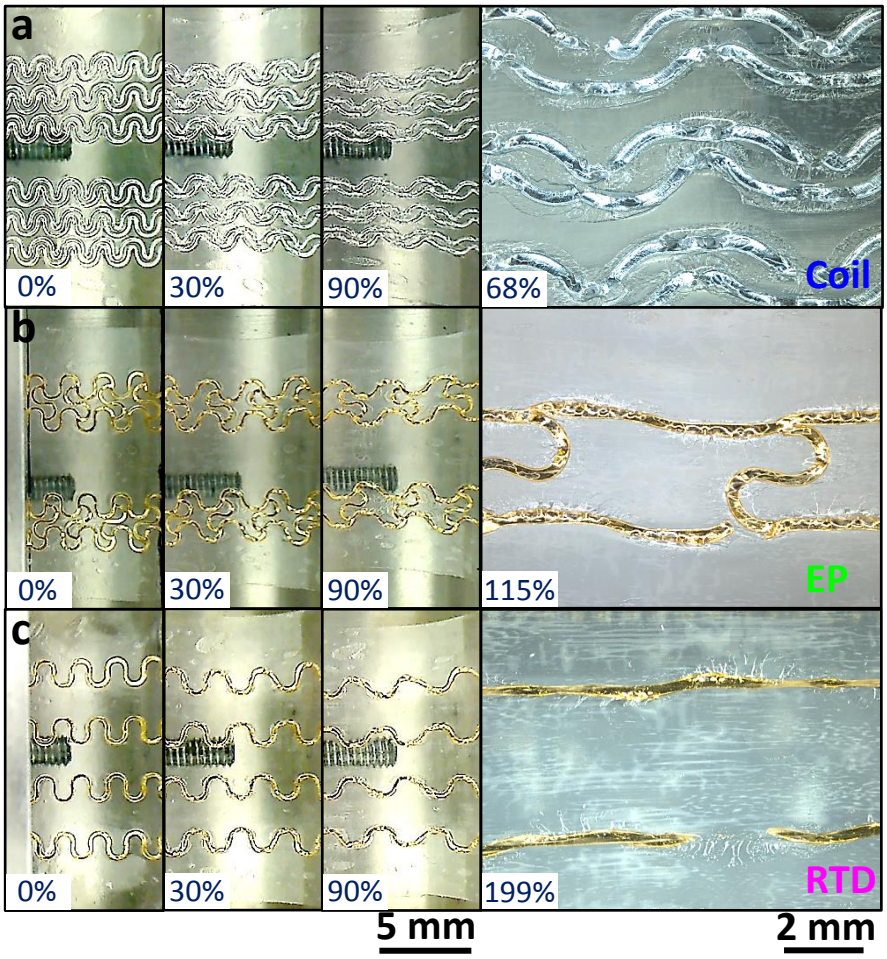

Figure S6: In situ images of different serpentine ribbons on Tegaderm stretched to certain strains. (**a**) Al coil serpentine at different applied strain up to its strain-to-rupture; (**b**) Au EP serpentine at different applied strain up to its strain-to-rupture; (**c**) Au RTD serpentine at different applied strain up to its strain-to-rupture.

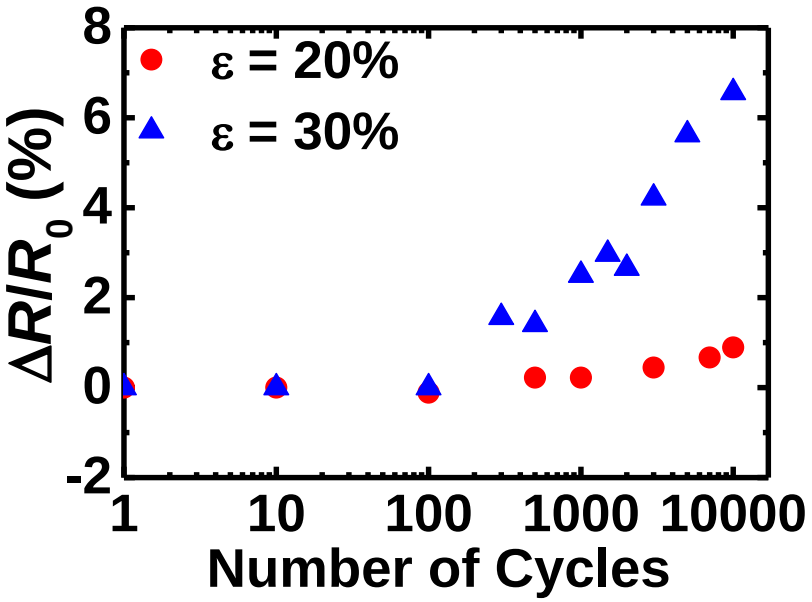

Figure S7: Cyclic test for RTD. Peak strain of 30% is applied on RTD and the resistance result shows the device is robust up to several hundreds number of cycles.

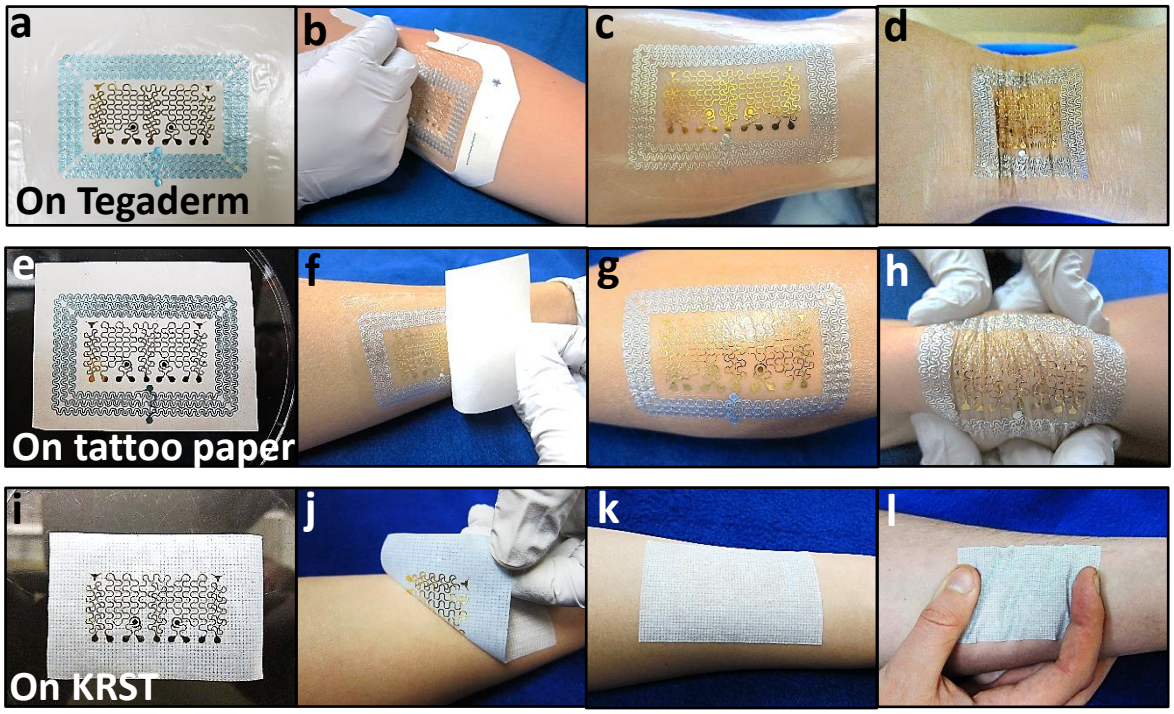

Figure S8: ESS on different substrates. (**a**) ESS on Tegaderm. (**b**) Applying ESS on the crook of the elbow. (**c**) As applied ESS. (**d**) ESS when elbow bends. (**e**) ESS on tattoo paper. (**f**) Applying ESS on forearm. (**g**) As applied ESS. (**h**) ESS under compression. (**i**) ESS on KRST. (**j**) Applying ESS on skin. (**k**) As applied ESS. (**l**) ESS under compression. ESS on Tegaderm and tattoo paper are not reusable but ESS on KRST is reusable as KRST is thick enough to stay flat after removal and the silicone adhesive remains effective after repeated use.

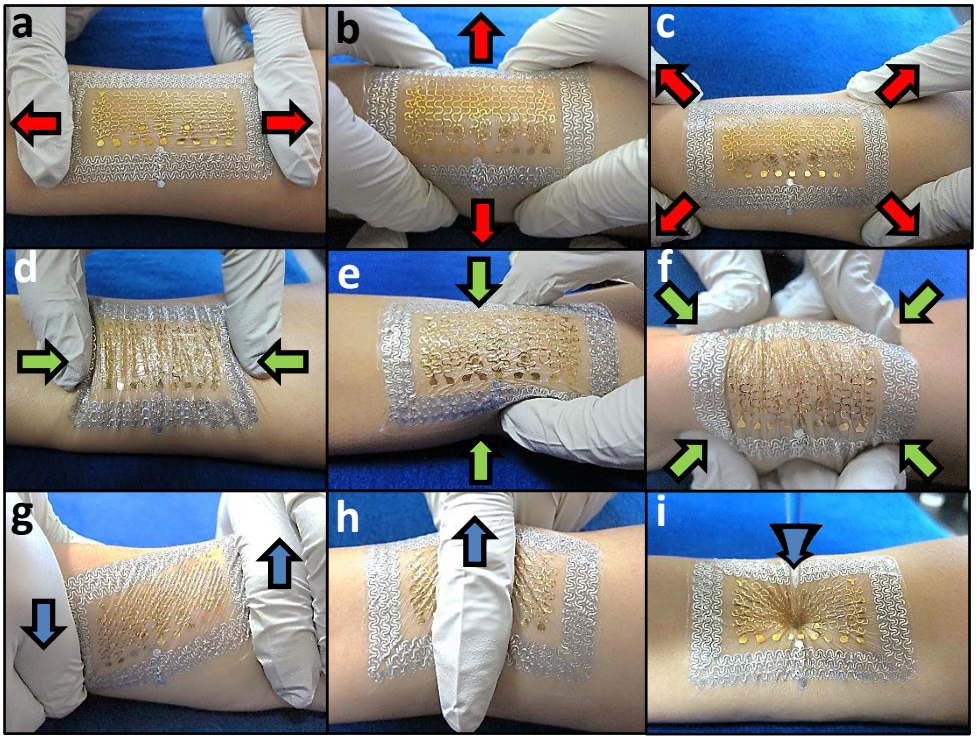

Figure S9: Deformability of ESS on human skin. Tattoo-paper supported ESS under (**a**) longitudinal stretch (**b**) transverse stretch (**c**) biaxial stretch (**d**) longitudinal compress (**e**) transverse compress (**f**) biaxial compress (**g**) shear (**h**) rub (**i**) poking by a glass rod.

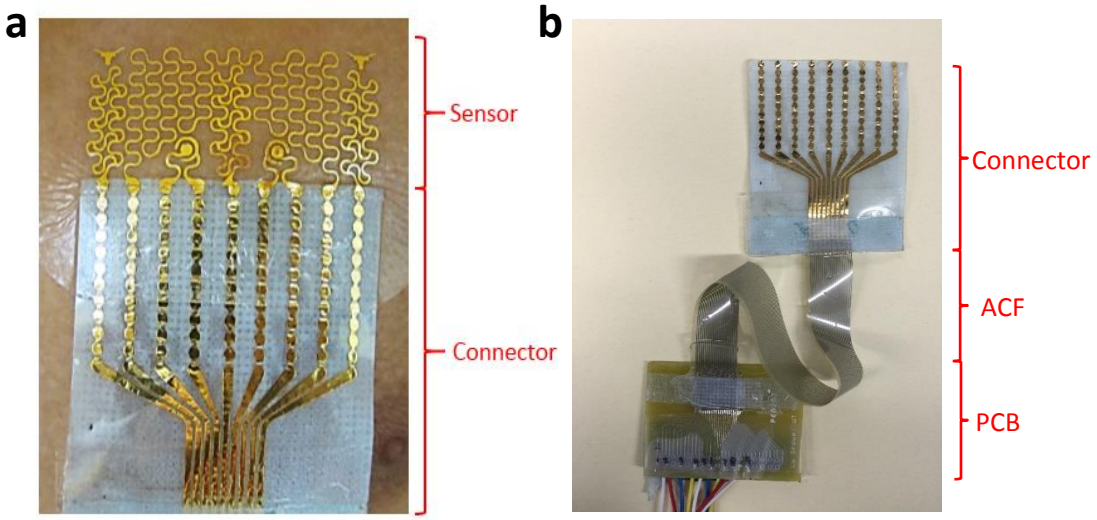

Figure S10: Homemade reusable connector for ESS. (**a**) A picture of ESS connected with the reusable connector which was also made by the cut-and-paste method. (**b**) The connector is linked to a printed circuit board (PCB) with soldered wires through anisotropic cohesive film (ACF).

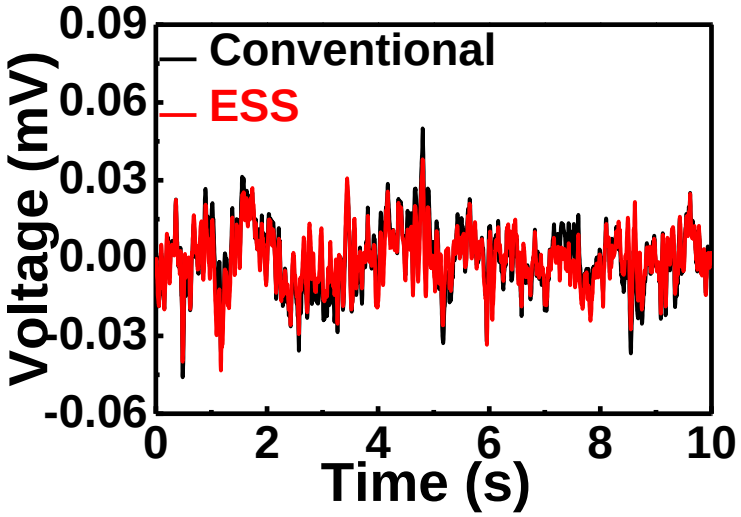

Figure S11: EEG simultaneously measured by gel Ag/AgCl electrode and Au serpentine EP on ESS with the electrode placement shown in Figure 3c left panel and FFT results shown in Fig. 3c right panel.

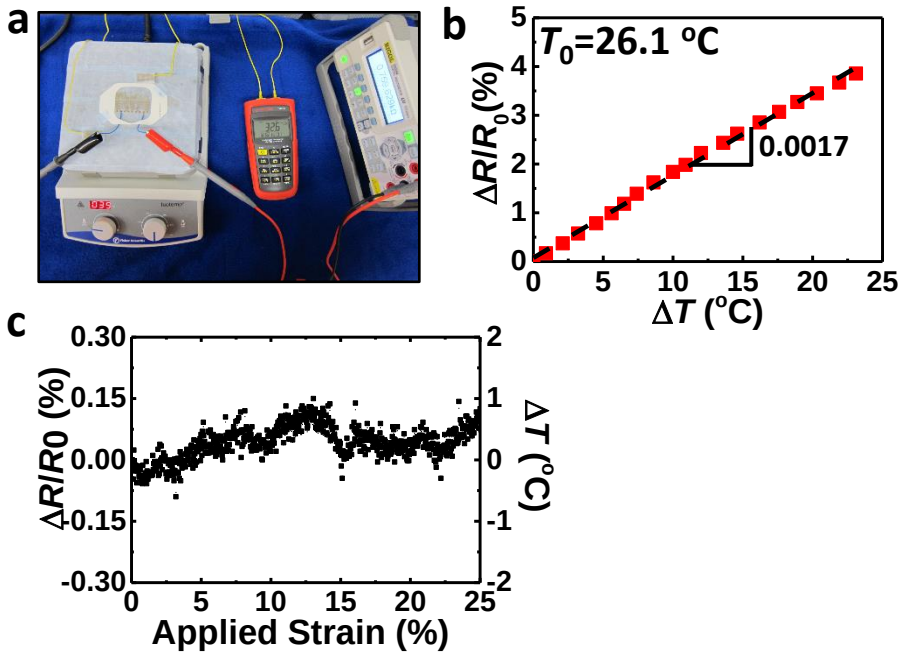

Figure S12: RTD calibration and strain sensitivity test. (**a**) Experimental setup to calibrate Au-PET based resistance temperature detector (RTD) using a thermocouple. (**b**) Calibration curve of RTD. The measured temperature coefficient of resistance is 0.0017. (**c**) When RTD is subjected to strain test, 25% tensile strain only leads to less than 0.01ºC temperature change, which validates that our stretchable RTD is strain insensitive.

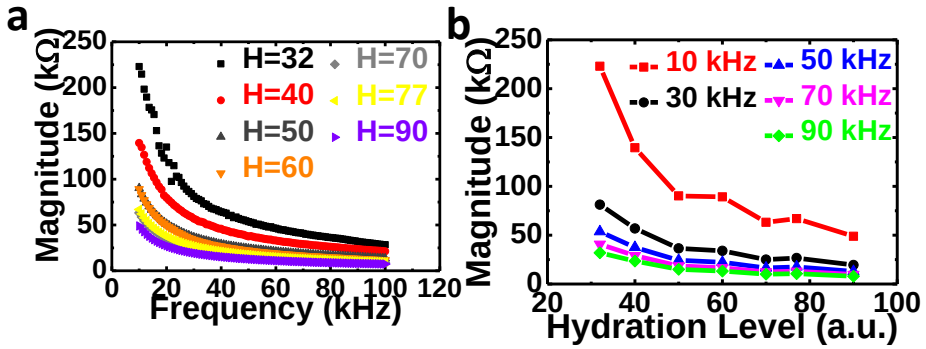

Figure S13: Skin hydration calibration. Calibration curves for hydration sensor measured on human skin. The magnitude of impedance is plotted as a function of (a) sweeping frequency and (b) hydration level.

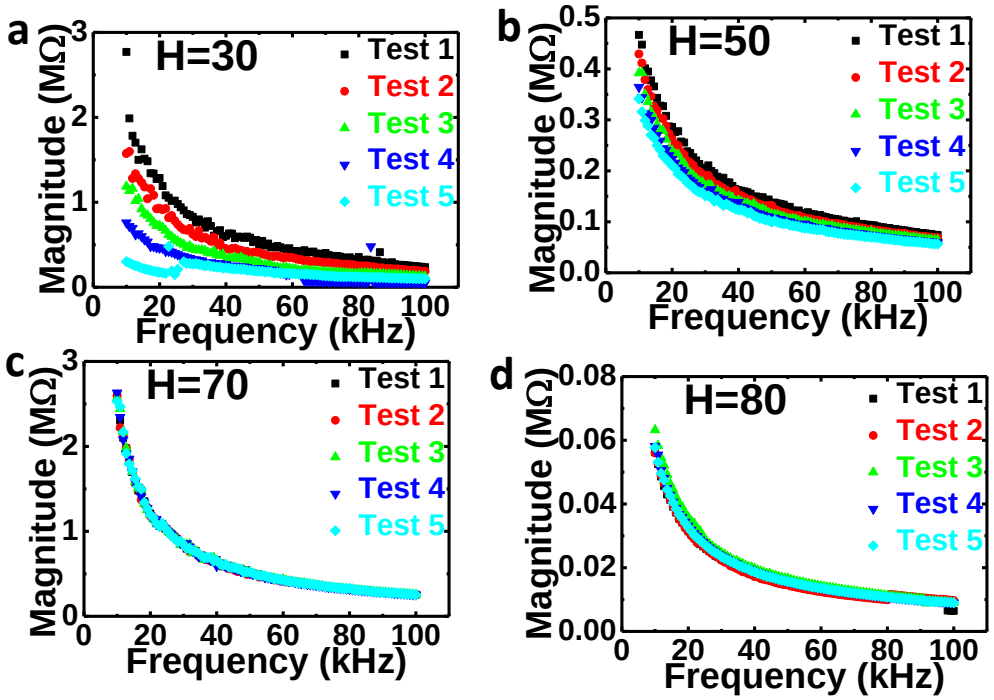

Figure S14: Sweating induced by ESS application on skin. Skin impedance was measured five consecutive times (34 sec. for each frequency sweep) immediately after applying the Tegaderm-supported ESS on human forearm. Initial skin hydration (H) was probed by commercial corneometer: (**a**) H = 30 (**b**) H = 50 (**c**) H = 70 (**d**) H = 80. When skin was dry (e.g. H = 30 or 50), skin impedance drops (hydration increases) right after ESS application but when skin was hydrated (e.g. H = 70 or 80 with applied moisturizer), impedance did not change after ESS application.

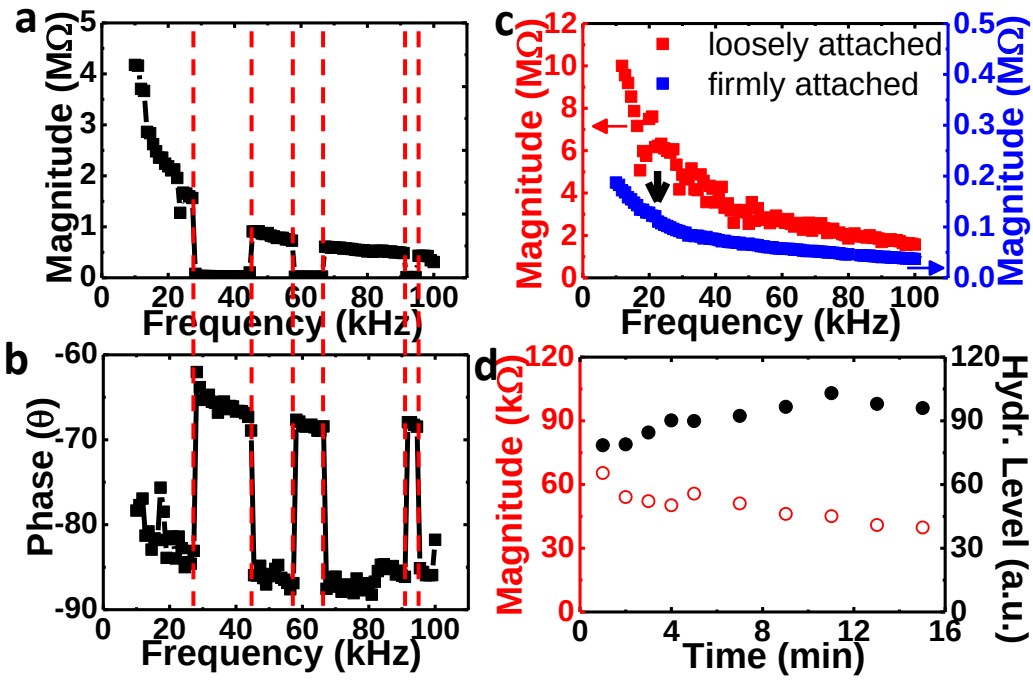

Figure S15: Effect of contact pressure on epidermal hydration sensor. (**a**) Magnitude of impedance and (**b**) phase change responding to repeated firm pressure applied on ESS which was gently attached on skin. (**c**) Magnitude of impedance without (red) and with (blue) one time hard press immediately after ESS was applied on skin. After one time hard press, magnitude drops orders of magnitude and pressure effect is eliminated. (**d**) Calibration of hard pressed hydration sensor. Red circles represent impedance measured by ESS and black dots represent hydration levels measured by commercial corneometer at the same spot.

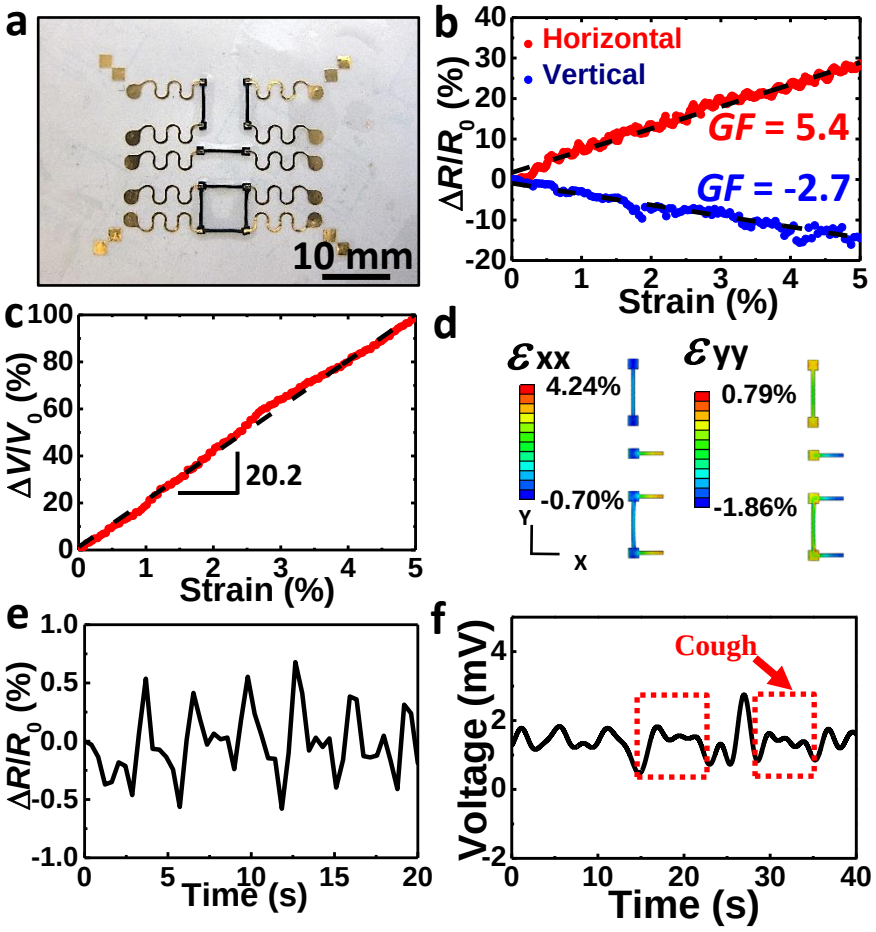

Figure S16: Stretchable strain gauges made by electrically conductive rubber (ECR) on ESS for respiratory rate and pattern monitoring. (**a**) Picture of the ESS strain gauge where ECR (black) is the strain sensing component and Au serpentine ribbons (yellow) serve as interconnects. Calibration curves for (**b**) horizontal and vertical ECR resistors and (**c**) Wheatstone bridge obtained by horizontal uniaxial tension tests. (**d**) FEM strain distribution in ECR when the supporting Tegaderm substrate is stretched horizontally by 5%. (**e**) Resistance of horizontal strain gauge indicates individual respiratory instants. (**f**) Voltage outputs from the ECR Wheatstone bridge during cough.

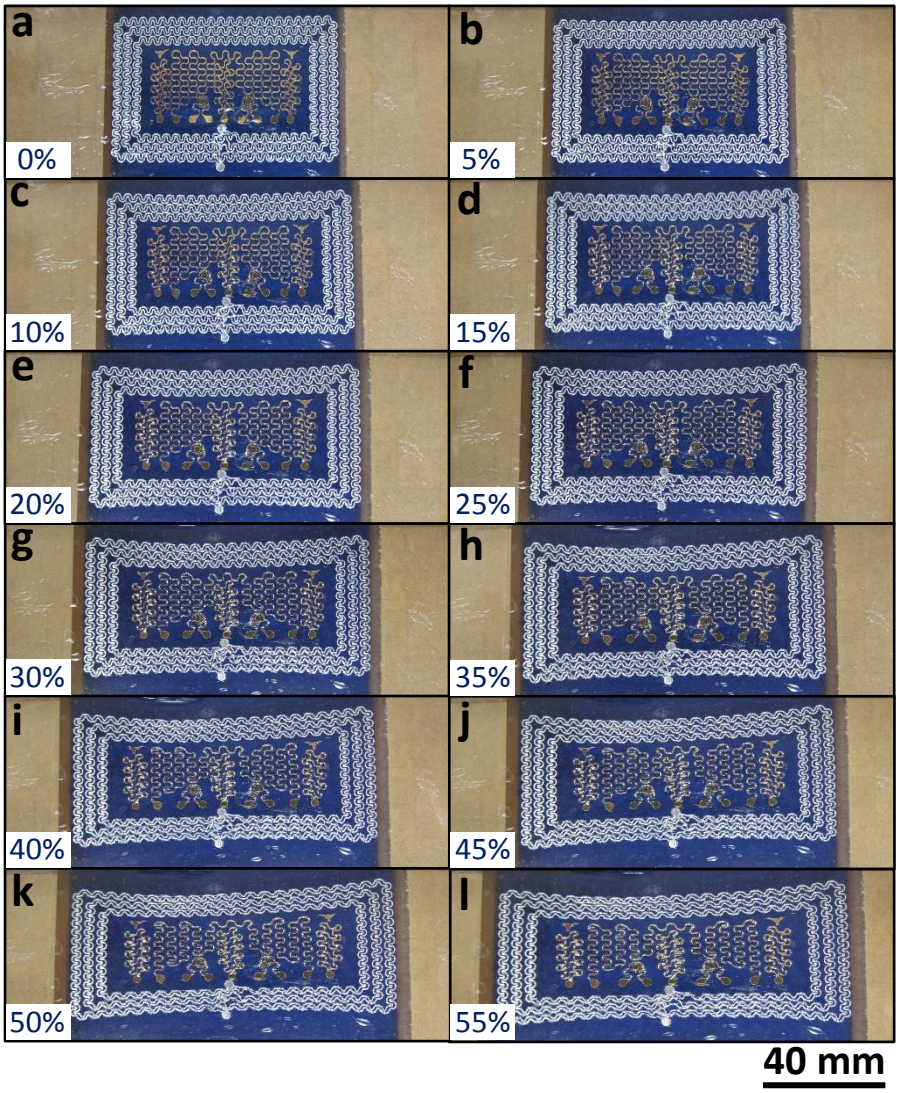

Figure S17: Images of Tegaderm-supported ESS under different uniaxial tension strain. The stretchability of our ESS is 55% with the Al coil ruptures first.

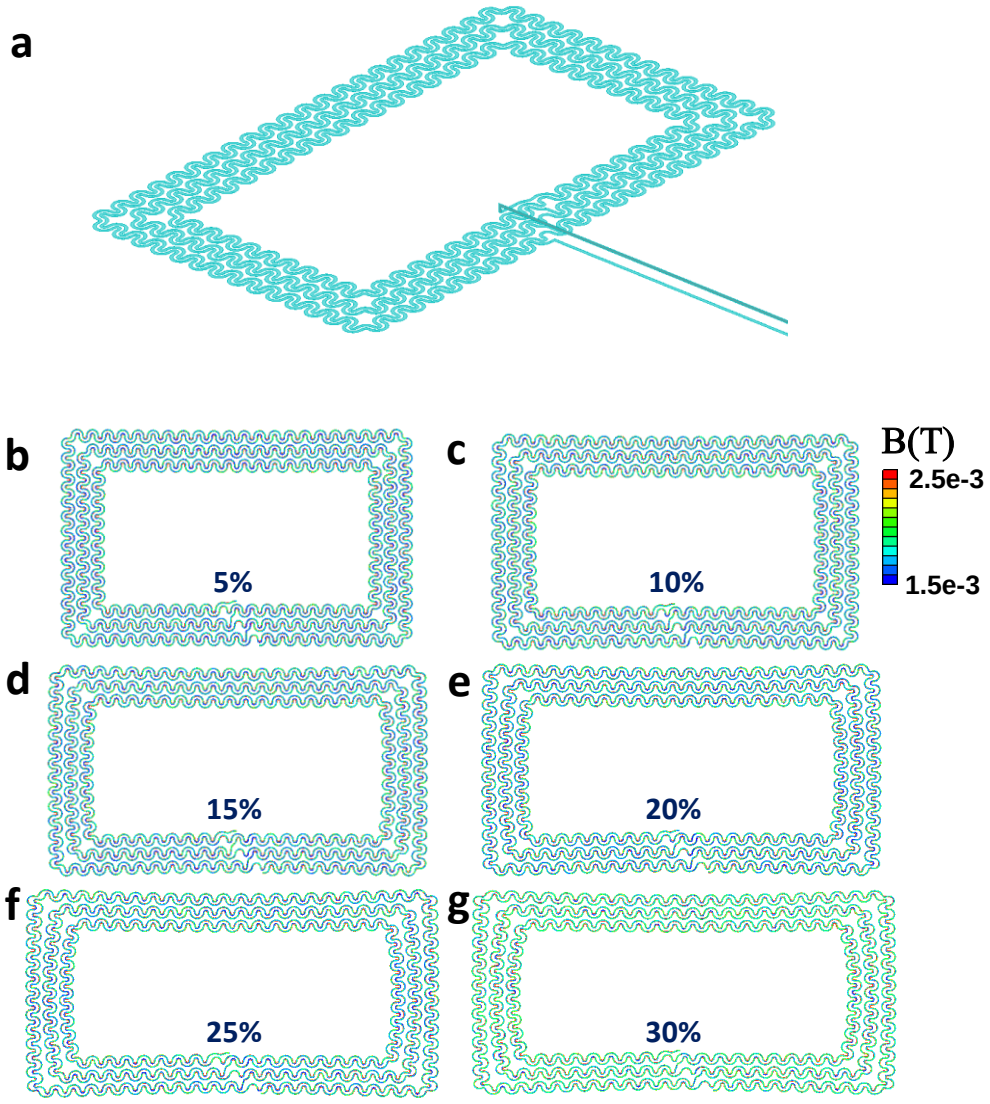

Figure S18: FEM of the inductance of the stretchable Al coil using ANSYS Maxwell. (**a**) 3D model of the coil with extension wire (atmosphere box is not showing). (**b**)-(**g**) Serpentine coil under different applied strains with contour plot of the magnetic (B) filed magnitude.

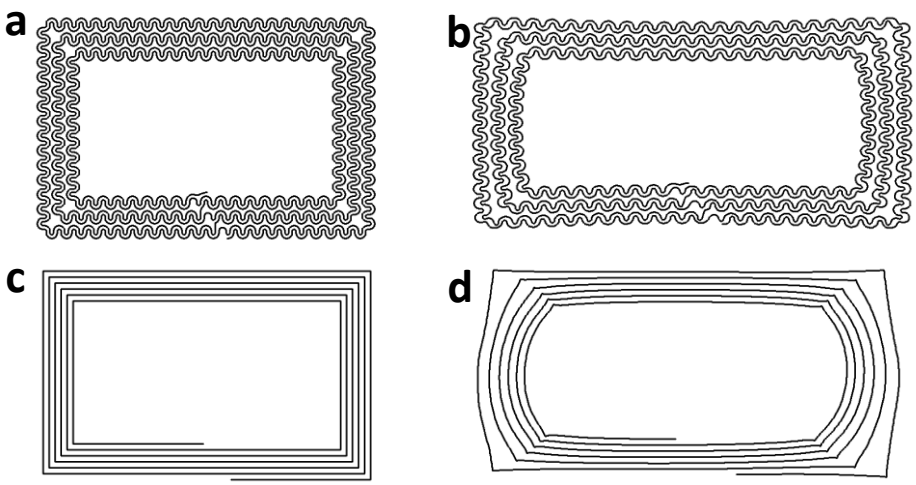

Figure S19: Deformed shapes of Tegaderm-supported serpentine and straight coils obtained by FEM. (**a**) Undeformed serpentine coil. (**b**) FEM result of the serpentine coil with 30% applied strain on Tegaderm. (**c**) Undeformed straight coil with the same number of turns as the serpentine coil. (**d**) FEM result of the straight coil with 30% applied strain on Tegaderm.

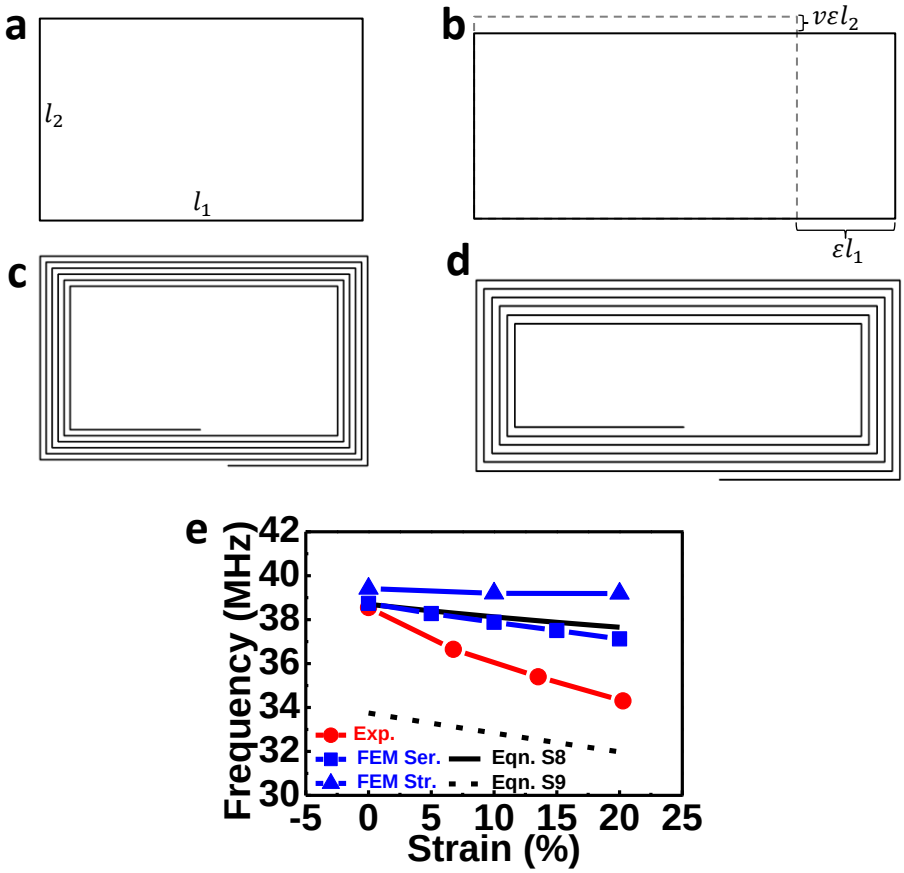

Figure S20: Analytical modeling of freestanding straight coils. (**a**) Undeformed single turn straight coil with initial length l_1 and l_2. (**b**) Single turn straight coil subjected to 30% applied strain. (**c**) Undeformed multi-turn straight coil. (**d**) Multi-turn straight coil artificially deformed by 30% uniformly. (**e**) Experimental (red), FEM (blue), and analytical (black) results show decreased resonance frequency with increased tensile strain.

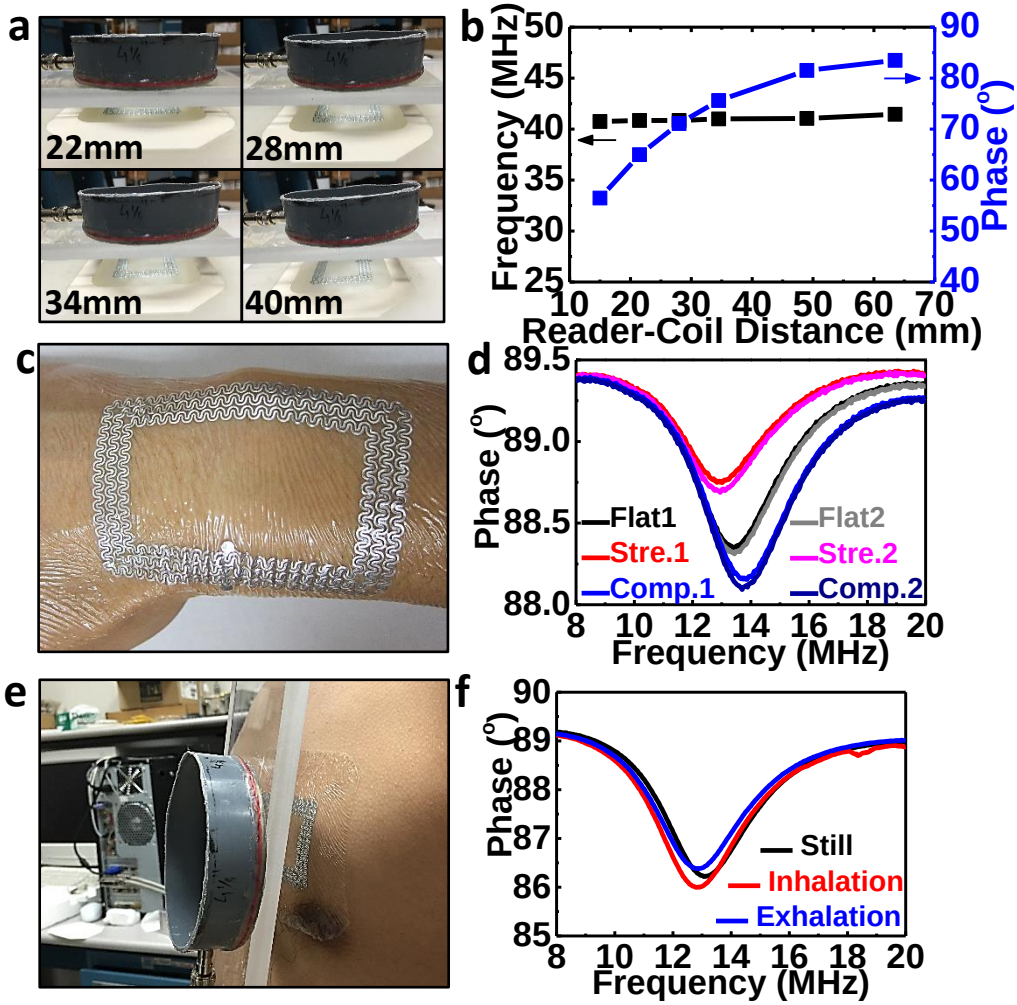

Figure S21: Effect of reader distance, repeatability, and strain sensitivity of the stretchable Al coil. (**a**) Images of different separation distance between reader and the Al coil. (**b**) Plots of resonance frequency (black) and phase (blue) as function of reader-coil distance. It shows the resonance frequency is unaffected by the reader-coil distance whereas the phase depends on it. (**c**) Images for on skin test of the Al coil. (**d**) Phase response as a function of sweeping frequency at repeated "flat", "stretch" and "compress" hand position. Good repeatability is observed. (**e**) Image for on-chest measurement. (**f**) Phase respond as a function of sweeping frequency at "still", "inhalation", and "exhalation" instant. It shows the resonance frequency and phase are stable in the three instants.